Article:
Madej, M, White, JBR, Nowakowska, Z et al. (10 more authors) (2020) Structural and functional insights into oligopeptide acquisition by the RagAB transporter from Porphyromonas gingivalis. Nature Microbiology, 5 (8). pp. 1016-1025. ISSN 2058-5276

https://doi.org/10.1038/s41564-020-0716-y

1
2 # 1. Extended Data
3
4

Figure #	Figure title One sentence only	Filename This should be the name the file is saved as when it is uploaded to our system. Please include the file extension. i.e.: *Smith_ED_Fig1.jpg*	Figure Legend If you are citing a reference for the first time in these legends, please include all new references in the Online Methods References section, and carry on the numbering from the main References section of the paper.
Extended Data Fig. 1	**Unbiased peptide density in RagAB**	EDFig1.tiff	Stereo diagrams showing 2Fo-Fc (**a**) and Fo-Fc density (**b**) in RagAB KRAB before any modelling and refinement of the peptide. Selected segments of RagA (cyan) and RagB (green) neighbouring the peptide are shown. Map contouring parameters are 1.0σ, carve = 2 for the 2Fo-Fc and 3.0σ, carve = 2 for the Fo-Fc map. The extensive contacts of RagA with the peptide are confirmed by a PISA interface analysis[17] which shows that 26 RagA residues form an interface with the peptide compared to only 8 for RagB, generating interface areas of 620 and 240 $Å^2$ with RagA and RagB respectively. The PISA CSS (complexation significance score) is maximal (1.0) for peptide-RagA while it is only 0.014 for peptide-RagB. This suggests that the observed co-crystal structure represents a state where the ligand has been partially transferred from an initial, presumably low(er)-affinity binding site on RagB to a high(er)-affinity binding site in the RagAB complex, allowing co-purification.
Extended Data Fig. 2	**RagAB binds a wide range of oligopeptides**	EDFig2.tiff	**a-c**, LC-MS/MS analysis of peptides bound to RagAB W83 KRAB, showing length distribution (**a**), total charge (**b**) and pI (**c**). **d-f**, Analysis of peptides

			bound to RagAB W83 wild-type, showing length distribution (**d**), total charge (**e**) and pI (**f**). For charge calculations, the pH was assumed to be 7.0 and contributions of any His residues were ignored. **g**, Amino acid frequency of RagAB-bound peptides (KRAB and wild-type combined; black) vs. the amino acid composition in the *P. gingivalis* proteome (gray), showing a substantial enrichment of Ala, Glu, Lys, Thr and Val. By contrast, aromatics (Phe, Trp) and bulky hydrophobics (Leu) appear to be under-represented. The peptides bound to RagAB from W83 KRAB vary in length from 7 to 29 residues, with a broad maximum of around 13 residues that fits well with the peptide density observed in the structures. Assuming equal abundance of each detected peptide, there is a slight preference for neutral to slightly acidic peptides, and the pI distribution has a bimodal shape, with maxima for acidic and slightly basic peptides. Analysis of the smaller RagAB-bound peptide set from wild-type W83 (**d-f**) yields a slightly wider size range from 5-36 residues, but overall there are no dramatic differences in the collective length, net charge and pI of the RagAB-bound peptide populations from W83 KRAB and wild-type strains.
Extended Data Fig. 3	**Molecular dynamics simulations of RagAB show lid opening**	EDFig3.tiff	**a**, C_α-rmsd values of RagB lids in apo-RagAB (red) and peptide-bound RagAB (green) with reference to the starting crystal structure in the closed conformation. The C_α-rmsd values of the RagB lids in $RagA_2B_2$ are shown in blue with reference to the OO EM state. Each point indicates an average of 50 ns simulation trajectory. **b**, Comparison of the $RagA_2B_2$ open conformation from EM (magenta)

			with the snapshot of the most open simulation at 2500 ns (green). **c**, Internal surface of peptide binding cavities in closed holo-RagAB and apo-RagAB, generated with CASTp[68]. The bound peptide from a RagAB subunit in the crystal structure was removed *in silico* to generate a closed apo-complex, and three independent MD simulations were performed. For one of the simulations, a clear opening of the RagB lid was observed, reminiscent of recent results for a SusCD transporter and supporting the notion that ligand removal resets the transporter to favour the open state[16]. None of the peptide-bound complexes shows lid opening on the timescale of the simulations. While this suggests that lid opening is less favourable in the ligand-bound state, it does not contradict our observation of open, ligand-bound complexes via EM. The EM structures allowed us to compare both open states, which showed that the RagB lid in the simulation opens less wide than that in the EM structure, at least during the timescale of the simulation. We also observed a partial closing of both RagB lids during a 1000 ns simulation starting from the OO EM state (**a**, blue curves). The r.m.s.d. values of both RagB subunits decrease from ~30 Å in the EM structure (t = 0 ns) to ~15 Å, which is similar to the opening observed in one of the apo-RagAB simulations starting from the closed structure. Thus, it appears that the energy minimum for the open state in the simulations is different from that in solution, for reasons that are not clear.
Extended Data Fig. 4	**RagB moves as a rigid body during**	EDFig4.tiff	**a**, Superposition of RagA subunits in the open (yellow) and closed (cyan) RagAB complexes in the

	lid opening		OC state, showing the rigid-body movement of RagB. Equivalent points are indicated by x,y,z (closed RagB; green) and by x*, y*, z* (open RagB; red). The arrow indicates the approximate pivot point in the N-terminus of RagB at the back of the complex. **b**, Superposition as in (**a**), viewed from the extracellular side. Lid opening results in displacements of up to 45 Å for main chain atoms at the front of the complex, furthest away from the RagB N-terminus. **c**, Superposition of the open and closed states of RagB, with the N-termini indicated. **d**, Extracellular view of superposed RagA, with selected loops labelled. The conformational changes upon lid movement are mostly confined to those parts of the protein that continue to interact with RagB at the back of the complex (L7-L9).
Extended Data Fig. 5	**Local resolution-filtered cryoEM maps and evidence for NTE density**	EDFig5.tiff	**a**, CC, OC and OO states of RagAB filtered and coloured by local resolution. Corresponding Fourier Shell Correlation (FSC) curves are shown (right). **b**, Unsharpened maps of RagAB displayed at low contour levels to reveal diffuse density attributed to the NTE. CC, OC and OO states are coloured purple, blue and green respectively.
Extended Data Fig. 6	**Analysis of RagAB mutants**	EDFig6.tiff	**a**, Representative growth curves (n = 3, mean ± standard error of the mean) for mutant W83 *ragAB* variants on BSA-MM. For comparison, W83 WT and Δ*ragAB* strains are shown as well. **b**, Representative SDS-PAGE gel (n = 2) showing OM protein expression levels following removal of inner membrane proteins by sarkosyl treatment. The $RagAB_{mono}$ and both RagA hinge loop mutant strains

			have a similar phenotype as ΔRagAB, suggesting they cannot take up oligopeptides produced by gingipains. However, the OM protein levels show that very little RagAB is present, so that no conclusions about functionality can be drawn. The RagB acidic loop mutants show intermediate growth on BSA-MM, suggesting that oligopeptide uptake is somewhat impaired. However, the OMP levels of the acidic loop mutants are substantially lower than wild type, suggesting that both acidic loop mutants are likely functional and arguing that the slow growth of *rag-4 P. gingivalis* strain ATCC 33277 on BSA-MM is not due to the absence of the acidic loop in RagB.
Extended Data Fig. 7	**RagAB and RagB bind peptides selectively**	EDFig7.tiff	MST titration curves with the P4-FAM peptide for (**a**) RagAB from ATCC 33277, (**b**) RagAB from W83 and (**c**) Omp40-41 from W83 (negative control). The other panels show MST profiles for unlabelled P21, P12 or P4 binding to His-tag labelled W83 RagAB (**d-f**) and His-tag labelled W83 RagB (**g-i**). Experiments and listed K_d values represent the mean of three independent experiments ± SD.
Extended Data Fig. 8	**Electron density comparison for different peptide ensembles**	EDFig8.tiff	**a**, Fo-Fc electron density maps (contoured at 3.0 σ) for the modelled peptide following final refinement for RagAB purified from W83 KRAB (left panel; 3.4 Å resolution), RagAB from W83 wild type co-crystallised with excess P21 peptide (middle panel; 2.6 Å), and RagAB from W83 wild type (right panel; 3.0 Å). Peptide sequence of the P21 co-crystal structure is arbitrarily modelled as QNGGANTSRGSAG, with numbering in italics according to the W83 KRAB peptide. Neighbouring residues D400-M407 of RagA are shown as cyan

			stick models for orientation purposes. **b**, Simulated annealing composite 2Fo-Fc omit maps for peptides bound to RagAB complexes as in (**a**). An annealing temperature of 500 K was used, with 5% of the models omitted. The fact that two different peptide ensembles produce similar maps as the P21 peptide, together with the inability to model the P21 sequence, suggests that the substrates are bound with register shifts and perhaps different chain directions. **c**, Stereo view of superposed 2Fo-Fc maps (made within Phenix; 1.0 σ, carve = 2.0) for WT RagAB in the absence (blue) and presence (orange) of P21 peptide, generated with the same high resolution cutoff (3.0 Å). For orientation purposes, the P21 peptide model is shown as sticks.
Extended Data Fig. 9	**Schematic demonstrating the proposed mechanism of substrate capture and translocation by RagAB**	EDFig9.tiff	Peptide ligands to be imported by the RagAB system are predominantly generated by the action of gingipains on serum and tissue-derived proteins. **1.** A lid-open state of RagAB permits peptide binding. **2.** Contributions from both RagA and RagB to peptide binding elicits closure of the lid, forming the transport-competent state of the complex. This is signalled across the OM by perturbation of the TonB box region on the periplasmic side of the plug domain, making it accessible to TonB. **3.** According to the literature consensus, TonB-mediated disruption of the plug permits substrate translocation and a return to the open state of RagAB.
Extended Data Fig. 10	**Cryo-electron microscopy data support substrate-induced lid closure in RagAB**	EDFig10.tiff	**a,b**, 3D classes for RagAB 'as purified' (**a**) and in the presence of 50-fold excess P21 peptide (**b**). Classes corresponding to the CC, OC and OO states are coloured purple, blue and green respectively. Junk or ambiguous classes *e.g.* where RagA barrels are

			incomplete are coloured grey. In the presence of P21 there was no clear OO state whilst the the proportion of the CC state increased, supporting the proposed mechanism of substrate capture.

2. Supplementary Information:

A. Flat Files

Item	Present?	Filename This should be the name the file is saved as when it is uploaded to our system, and should include the file extension. The extension must be .pdf	A brief, numerical description of file contents. i.e.: *Supplementary Figures 1-4, Supplementary Discussion, and Supplementary Tables 1-4.*
Supplementary Information	Yes	SI-final.pdf	Supplementary Figures 1-3, Supplementary Tables 1-4, Supplementary Movie legend
Reporting Summary	Yes		

B. Additional Supplementary Files

Type	Number If there are multiple files of the same type this should be the numerical indicator. i.e. "1" for Video 1, "2" for Video 2, etc.	Filename This should be the name the file is saved as when it is uploaded to our system, and should include the file extension. i.e.: *Smith_*	Legend or Descriptive Caption Describe the contents of the file

		Supplementary_Video_1.mov	
Supplementary Video		RagAB-movie.mp4	**Supplementary Movie** Dynamics of the RagAB transporter. Cryo-EM map of open-closed (OC) RagAB, with cartoon models shown for RagA (blue) and RagB (yellow or grey) subunits.
Supplementary Data		RagAB-peptidomics.xlsx	**Supplementary Table 2** RagAB peptidomics and *in vitro* binding of peptides to RagAB and RagB. Both analyses contain two separate Excel spreadsheets: all information retrieved from Mascot (Mascot) and a reduced spreadsheet with summed spectra (duplicates) and one charge variant of each peptide (Spectral C.) For spectral C., additional statistics were calculated: Spectral count peptide - summed number of

			spectra of particular peptide; Spectral count protein - summed number of spectra per particular protein; Spectral count sample - summed number of spectra per particular sample; Ratio peptide/protein - ratio of total number of particular peptide spectra to total number of spectra per protein; Ratio peptide/sample - ratio of total number of particular peptide spectra to total number of spectra per protein.

3. Source Data

Figure	Filename This should be the name the file is saved as when it is uploaded to our system, and should include the file extension. i.e.: *Smith_SourceData_Fig1.xls,* or *Smith_*	Data description i.e.: Unprocessed Western Blots and/or gels, Statistical Source Data, etc.

	Unmodified_Gels_Fig1.pdf	
Source Data Fig. 1	Uncropped-Fig1a.pdf	Unprocessed SDS-PAGE gel for Fig. 1a
Source Data Fig. 4	Source_Data-Fig4.xlsx	Excel spreadsheet with source data for Fig. 4
Source Data Extended Data Fig. 2	Source_Data-EDFig2.xlsx	Excel spreadsheet with source data for ED Fig. 2
Source Data Extended Data Fig. 6	Source_Data-EDFig6a.xlsx	Excel spreadsheet with source data for ED Fig. 6a
Source Data Extended Data Fig. 6	Uncropped-EDFig6b.pdf	Unprocessed SDS-PAGE gel for ED Fig. 6b
Source Data Extended Data Fig. 7	Source_Data-EDFig7.xlsx	Excel spreadsheet with source data for ED Fig. 7

Structural and functional insights into oligopeptide acquisition by the RagAB transporter from *Porphyromonas gingivalis*

Mariusz Madej[1,2*], Joshua B. R. White[3*], Zuzanna Nowakowska[1], Shaun Rawson[3‡], Carsten Scavenius[4], Jan J. Enghild[4], Grzegorz P. Bereta[1], Karunakar Pothula[5], Ulrich Kleinekathoefer[5], Arnaud Baslé[7], Neil Ranson[3#], Jan Potempa[1,6#], Bert van den Berg[7#]

[1]Department of Microbiology, Faculty of Biochemistry, Biophysics and Biotechnology, Jagiellonian University, 30-387 Krakow, Poland

[2]Malopolska Centre of Biotechnology, Jagiellonian University, 30-387 Krakow, Poland

[3]Astbury Centre for Structural Molecular Biology, Faculty of Biological Sciences, University of Leeds, Leeds, LS2 9JT, UK.

[4]Interdisciplinary Nanoscience Center (iNANO), and the Department of Molecular Biology, Aarhus University, Aarhus, DK-8000, Denmark

[5]Department of Physics and Earth Sciences, Jacobs University Bremen, Campus Ring 1, 28759 Bremen, Germany

[6]Department of Oral Immunology and Infectious Diseases, University of Louisville School of Dentistry, Louisville, KY40202, USA

[7]Biosciences Institute, The Medical School, Newcastle University, Newcastle upon Tyne NE2 4HH, UK.

[‡] Present address: The Harvard Cryo-Electron Microscopy Center for Structural Biology, Harvard Medical School, Boston, MA, USA.

* Authors contributed equally

Correspondence to: n.a.ranson@leeds.ac.uk
jan.potempa@icloud.com
bert.van-den-berg@ncl.ac.uk (lead contact)

Abstract

Porphyromonas gingivalis, an asaccharolytic member of the *Bacteroidetes*, is a keystone pathogen in human periodontitis that may also contribute to the development of other chronic inflammatory diseases. *P. gingivalis* utilizes protease-generated peptides derived from extracellular proteins for growth, but how those peptides enter the cell is not clear. Here we identify RagAB as the outer membrane importer for peptides. X-ray crystal structures show that the transporter forms a dimeric $RagA_2B_2$ complex, with the RagB substrate-binding surface-anchored lipoprotein forming a closed lid on the RagA TonB-dependent transporter. Cryo-electron microscopy structures reveal the opening of the RagB lid and thus provide direct evidence for a "pedal bin" nutrient uptake mechanism. Together with mutagenesis, peptide binding studies and RagAB peptidomics, our work identifies RagAB as a dynamic, selective OM oligopeptide acquisition machine that is essential for the efficient utilisation of proteinaceous nutrients by *P. gingivalis*.

Introduction

The Gram-negative Bacteroidetes are abundant members of the human microbiota, especially in the gut. Outside the gut, Bacteroidetes often cause disease, with the best-known examples being the oral Bacteroidetes *Porphyromonas gingivalis* and *Tannerella forsythia* that are part of the "red complex" involved in periodontitis[1], the most prevalent infection-driven chronic inflammation in the Western world[2]. Accumulating evidence suggests a link between periodontitis and other chronic inflammatory diseases, including rheumatoid arthritis, Alzheimer's disease, chronic obstructive pulmonary disease and cardiovascular disease[3-7]. Given this link, and its fastidious growth requirements, it is important to understand how *P. gingivalis*, thrives and causes dysbiosis of the oral microbiota, leading to inflammation and periodontal tissue destruction.

Unlike many human gut Bacteroidetes that specialise in degrading glycans, *P. gingivalis* is asaccharolytic and exclusively utilises peptides for growth[8]. Those peptides are generated by multiple proteases[9,10], the best-known of which are the gingipains. These large and abundant surface-anchored cysteine endoproteases possess cumulative trypsin-like activity, and are essential for *P. gingivalis* virulence and growth on proteins as the sole source of carbon[11]. Crucially, it is not clear how gingipain-generated peptides are taken up by *P. gingivalis*, although a role for the RagAB outer membrane (OM) protein complex has been proposed[12]. RagAB consists

93 of a TonB dependent transporter (TBDT) RagA (PG_0185) and a substrate-binding surface
94 lipoprotein RagB (PG_0186). However, a recent crystal structure of *P. gingivalis* RagB was
95 claimed to contain bound monosaccharides[13], and a role in polysaccharide utilisation was
96 proposed based on sequence similarity with SusCD systems from gut Bacteroidetes[13-15]. Recent
97 structures suggest that SusC and SusD proteins from *Bacteroides thetaiotaomicron* form stable
98 dimeric complexes ($SusC_2D_2$), with SusD capping the extracellular face of the SusC transporter.
99 Molecular dynamics (MD) simulations and electrophysiology studies led to the proposal that
100 nutrient uptake likely occurs via a hinge-like opening of the SusD lid, a so-called pedal bin
101 mechanism[16]. However, the molecular details of nutrient acquisition by SusCD-like complexes
102 remain unclear, as do any differences between putative OM peptide and glycan transporters.
103
104 Here we report integrated structural and functional studies of RagAB purified from *P. gingivalis*
105 W83 via X-ray crystallography and cryo-electron microscopy (cryo-EM). The crystal structure
106 shows a dimeric $RagA_2B_2$ complex in which RagB caps the RagA transporter, forming a large
107 internal chamber that is occupied by co-purified bound peptides. Remarkably, and in sharp
108 contrast to the crystal structure of RagAB (and indeed of SusCDs), cryo-EM reveals large
109 conformational changes, with three distinct states found in a single dataset of the detergent-
110 solubilized $RagA_2B_2$ transporter. Together with RagAB peptidomics, structure-based site-directed
111 mutagenesis, and peptide binding studies, we show that RagAB is a dynamic OM oligopeptide
112 acquisition machine, with considerable substrate selectivity that is essential for the efficient
113 utilisation of protein substrates by *P. gingivalis*.
114

115 ## Results

116 ### Purification and X-ray crystal structure determination of RagAB from *P. gingivalis*

117 Since RagA does not express in the *E. coli* OM, we purified RagAB directly from *P. gingivalis* W83
118 KRAB (Δ*kgp*/Δ*rgpA*/Δ*rgpB*). This strain lacks gingipains, reducing proteolysis of many OM
119 proteins. RagAB is one of the most abundant OM proteins in *P. gingivalis*, and with the exception
120 of the 230 kDa Hemagglutinin A (HagA), no co-purifying proteins are present (Fig. 1a). This
121 indicates that the RagAB complex represents the complete transporter. Diffracting crystals were
122 obtained by vapour diffusion, and the structure was solved by molecular replacement using data to
123 3.4 Å resolution (Methods and Supplementary Table 1).
124
125 RagAB is dimeric ($RagA_2B_2$), with the same subunit arrangement and architecture (Fig. 1)
126 observed in two SusCD complexes from *Bacteroides thetaiotaomicron*[16]. RagB caps RagA,
127 burying an extensive surface area (~3800 $Å^2$) and forming a large, closed internal cavity which
128 contains clearly resolved density for an elongated, ~40 Å long molecule that is bound at the RagAB
129 interface (Extended Data Fig. 1). The electron density strongly suggests that the bound molecule is
130 a peptide of ~13 residues in length (Figs. 1d-g), although most side chains are truncated after the

131 Cβ or Cγ positions. Exceptions are residues 9-10 of the peptide, where well-defined side chain
132 density comes close to residues D99/D101 in RagB. The main chain of the peptide has somewhat
133 higher average B-factors than the neighbouring RagA (~95 A^2 and 73 A^2 respectively), suggesting
134 that it corresponds to an ensemble of different peptides with similar backbone conformations,
135 hereafter referred to as "the peptide". We modelled the peptide arbitrarily as
136 A^1STTG^{5}ANSQR^{10}GSG^{13} (Fig. 1e), which decreased the R_{free} of the model by about 0.25%. D99
137 and D101 of RagB are part of an acidic loop insertion (Asp^{99}-Glu-Asp-Glu^{102}) into an α-helix in
138 RagB's ligand binding site that protrudes into the RagAB binding cavity (Fig. 1g). The acidic nature
139 of this loop suggests that *P. gingivalis* W83 RagAB may prefer to take up basic peptides.
140 Interestingly, this acidic loop is absent in several RagB orthologs, including that from strain ATCC
141 33277 (Supplementary Figs. 1 and 2). Several RagAB residues likely form hydrogen bonds with
142 the backbone of the peptide (Fig. 1e), e.g. the side chain of N894 in RagA forms hydrogen bonds
143 with residues 6 and 8 of the peptide, and may therefore be important for substrate binding.
144 Collectively, RagAB residues interact with the backbone of 8 out of the 13 visible peptide residues,
145 and most of those interactions are provided by RagA.
146
147 To confirm the presence of co-purified peptides in RagAB we employed a LC-MS/MS peptidomics
148 approach. RagAB from W83 KRAB was associated with several hundred unique peptides
149 (Supplementary Table 2) with none present in the negative control Omp40-41 sample (Methods),
150 confirming our structure-based hypothesis that RagAB contains an ensemble of peptides. The
151 peptides originate mostly from abundant *P. gingivalis* proteins representing all cellular
152 compartments. As a comparison, we also analysed peptides bound to RagAB purified from the
153 gingipain-expressing W83 wild-type strain. This complex is identical to that of the KRAB strain but,
154 due to gingipain activity, the RagAB-associated peptides in wild-type W83 are different from those
155 in the gingipain-deficient KRAB strain (Supplementary Table 2). Any in-depth analysis of RagAB-
156 bound peptides is difficult because of the non-quantitative nature of MS. Assuming equal
157 abundance of each detected peptide, there are no dramatic differences in length distribution, pI
158 profiles and amino acid frequencies within the RagAB-bound peptides from W83 KRAB and wild-
159 type strains (Extended Data Fig. 2).
160
161 **Conformational changes in RagAB**
162 The crystal structure of RagAB is very similar to previously determined SusCD structures. Both
163 TBDT barrels are closed on the extracellular side by their RagB (or SusD) caps, even when no
164 substrate is bound[16]. This suggests either that the closed state is energetically favourable, or that
165 crystallisation selects for closed states from a wider conformational ensemble. We therefore
166 investigated the structure of detergent-solubilized RagAB in solution using single particle cryo-EM.
167 RagAB is unambiguously dimeric in solution. Strikingly, following initial 2D classification it was
168 immediately apparent that multiple conformations of the $RagA_2B_2$ dimer were present, and after

169 further classification steps, three distinct conformations were identified. Following 3D
170 reconstruction and refinement, three structures were obtained at near-atomic resolution,
171 corresponding to the three possible combinations of open and closed dimeric transporters: closed-
172 closed (CC; 3.3 Å), open-closed (OC; 3.3 Å) and open-open (OO; 3.4 Å) (Figs. 2 and 3;
173 Supplementary Table 3).
174
175 The CC state is essentially identical to the X-ray crystal structure (backbone r.m.s.d. values of ~0.6
176 Å), and the bound peptide occupies the same position. In the OO state, each RagB lid has
177 undergone a substantial conformational rearrangement that swings RagB upward, exposing the
178 peptide binding site and plug domain within the barrel interior. The bound peptide is present in both
179 barrels of the OO state, at the same position as in the CC state, but the density is weaker (Fig. 3),
180 suggesting lower occupancy or greater mobility for the bound peptide in the open state. The
181 presence of peptide in open complexes is consistent with a PISA interface analysis[17] that shows
182 the observed peptide binding site is mainly formed by RagA.
183
184 The most interesting state is the open-closed transporter (OC), in which the internal symmetry of
185 the $RagA_2B_2$ complex is broken. The density for bound peptide in the open barrel of the OC RagAB
186 is much weaker than in either barrel of the OO state (Fig. 3) even when both maps are generated
187 without symmetry, suggesting cross-talk between RagAB units. The OC state unambiguously
188 shows that the RagB lids in the dimeric complex can open and close separately. Fascinatingly, no
189 "intermediate" states in the opening of the transporter are observed: essentially all of the individual
190 RagAB pairs are either open or closed, and these are dimerised to give each of the three possible
191 states observed (CC, OC and OO). This suggests that either the dynamics of lid opening and
192 closing are very rapid, and/or that the energy landscape for opening and closing is very rugged,
193 with distinct stable minima only existing for the three discrete states observed here. MD
194 simulations performed prior to obtaining the EM structures show a similar, albeit less wide opening
195 of the RagB lid upon removal of the peptide (Extended Data Fig. 3). Superposition of the RagA
196 subunits of the open and closed states reveals that the N-terminal ~10 residues of the RagB lid
197 and the lipid anchor at the back of the complex remain stationary during lid opening (Extended
198 Data Fig. 4), acting as a hinge about which the rest of the protein moves as a rigid body
199 (Supplementary Movie).
200
201 **The open-closed complex reveals changes in the RagA plug domain**
202 In the consensus model of TonB-dependent transport[14], extracellular substrate binding induces a
203 conformational change that is transmitted through the plug domain of the TBDT and results in
204 disordering of its N-terminal Ton box. This increases accessibility of the Ton box from the
205 periplasm, permitting interaction with TonB in the inner membrane. The disordered state of the Ton
206 box can therefore be considered a signal, ensuring that only substrate-loaded transporters form

207 productive complexes with TonB, avoiding futile transport cycles. In crystal structures of TBDTs,
208 Ton box conformation varies. Where visible, this region interacts with other parts of the plug
209 domain and is assumed to be inaccessible to TonB. In other structures, electron density for the
210 Ton box is missing, indicating increased mobility. Importantly, the correlation between ligand
211 binding and visibility of the Ton box is poor[18], likely owing to crystallisation[19]. In contrast, the OC
212 state observed by cryo-EM provides an unbiased structure that relates ligand binding site
213 occupancy to changes in the plug domain (Fig. 3). In the open side, the first visible residue is Q103
214 at the start of the TonB box, whereas in the closed side (and in the crystal and CC EM structures),
215 the density starts at L115. The conformation of L115-S119 is also different from that in the open
216 complex, with shifts for L115 as large as 10 Å (Fig. 3d). Interestingly, the plug region A211-A219 is
217 also different in the two states. Notably, the pronounced shift for R218 (~9 Å for the head group;
218 Fig. 3e) may be important given its location at the bottom of the binding cavity. A211-A219
219 contacts the region following the Ton box, highlighting a potential allosteric route to communicate
220 binding site occupancy to the Ton box. This is a mechanism that would be consistent with previous
221 AFM data suggesting that the plugs of TBDTs consist of two domains[20] : an N-terminal, force-labile
222 domain that is removed by TonB to form a channel and a more stable C-terminal domain that
223 would include R218 in RagA. The difference in dynamics of the N-terminus of RagA is most
224 evident in unsharpened maps of the OC state contoured at low levels, which clearly show globular
225 density connected to the plug domain only in the open state (Extended Data Fig. 5). This density
226 corresponds to an ~80-residue N-terminal extension (NTE; Pfam 13715, Carboxypeptidase D
227 regulatory-like domain) that is present in a relatively small subset of TBDTs[21] and which precedes
228 the Ton box. In the closed state, the NTE and Ton box are not resolved in the cryo-EM maps,
229 presumably because of increased mobility.
230
231 **RagAB is important for growth of *P. gingivalis* on proteins as carbon source**
232 We initially assessed whether the *P. gingivalis* strains W83 and ATCC 33277 (hereafter named
233 ATCC) could grow on minimal medium supplemented with BSA as a sole carbon source (BSA-
234 MM; Methods). Interestingly, while growth on rich medium is identical, robust growth on BSA-MM
235 is observed only for the *rag-1* locus W83 strain[22]. By contrast, the *rag-4* strain ATCC grows slowly,
236 and after a substantial lag phase (Figs. 4a,c). Given the high sequence similarity of the RagA and
237 RagB proteins (Supplementary Figs. 1 and 2), the distinct growth profiles of W83 and ATCC
238 suggest that relatively small differences in RagAB could alter substrate uptake sufficiently to
239 dramatically affect growth on the relatively small set of peptides that can be generated from BSA.
240
241 To further investigate potential functional differences between the RagAB complexes from W83
242 and ATCC we constructed an ATCC strain in which W83 *ragAB* was expressed from a single-copy
243 plasmid in the ATCC *ΔragAB* background. We also made a strain in which the genomic copy of
244 ATCC *ragB* was replaced by W83 *ragB*. Remarkably, replacement of either RagB or RagAB from

245 ATCC with the corresponding orthologs from W83 results in robust growth of ATCC on BSA-MM
246 (Fig. 4c). Since the OM levels of RagAB for all strains are similar (Fig. 4d), these results have
247 several important implications. Firstly, they confirm that RagAB is required for growth on
248 extracellular protein-derived oligopeptides. Secondly, they suggest that different RagB lipoproteins
249 can form functional complexes with the same RagA transporter. Finally, and perhaps most
250 surprisingly, RagB appears to determine the substrate specificity of the complex. We speculate
251 that TonB-dependent transporters such as SusC and RagA may have acquired SusD and RagB
252 substrate binding lipoproteins to confer substrate specificity.
253
254 The long lag phase during growth of ATCC on 1% BSA-MM is consistent with previous data
255 showing that this strain requires either high substrate concentrations (3% BSA) or supplementation
256 with rich medium for growth on BSA or human serum albumin (HSA) [23-25]. This may seem
257 surprising, given that HSA is an abundant component of gingival crevicular fluid (GCF), an
258 inflammatory exudate which is dominated by abundant plasma proteins such as albumin[26].
259 However, GCF does also contain many other proteins that could be substrates for ATCC, and
260 many other bacteria are present and could generate different substrates from those proteins. Thus,
261 slow growth on a single substrate *in vitro* does not translate to poor fitness *in vivo*. Poor growth on
262 BSA also does not imply that ATCC RagAB does not take up any BSA peptides, as the phenotype
263 could be caused by inefficient uptake of a particular BSA peptide that provides one or more
264 essential amino acids. Our Supplementary Table 2 identifies only 63 BSA-derived peptides after
265 trypsin digest, so the substrate pool is relatively small. This notion is supported by previous data
266 showing that while ATCC efficiently cleaves human albumin, transferrin, immunoglobulin G and
267 collagen, the two latter substrates don't support growth[24].
268
269 To better define the role of RagAB in peptide utilisation, we constructed clean deletions in *P.*
270 *gingivalis* W83 for *ragA*, *ragB*, and *ragAB* and grew the resulting strains on BSA-MM. Compared
271 to wild-type W83 RagAB, growth of the *ragA* and *ragAB* deletion strains exhibits long (~15-20 hrs)
272 lag periods (Fig. 4a). Unlike the gingipain-*null* KRAB strain[11], both mutant strains grow eventually,
273 most likely due to passive, RagAB-independent uptake of small peptides produced after prolonged
274 BSA digestion. Interestingly, the Δ*ragB* strain grows better on BSA than the Δ*ragAB* strain. Since
275 the strain still produces RagA (albeit at very low levels; Fig. 4b and Extended Data Fig. 6) this
276 demonstrates that RagB, in contrast to RagA, is not required for growth on BSA-derived
277 oligopeptides *in vitro*, in accordance with previous work[12]. Collectively, the growth data suggest
278 that RagAB mediates uptake of extracellular oligopeptides produced by gingipains, and help
279 explain data showing that the transporter is important for *in vivo* fitness and virulence of *P.*
280 *gingivalis*[22,27].
281

282 We next constructed mutant strains for structure-function studies (see Methods), and tested growth
283 on BSA-MM (Figs. 4a and Extended Data Fig. 6). Most mutant strains show very low OM levels of
284 RagAB, complicating conclusions about functionality (Extended Data Fig. 6). Exceptions are the
285 Ton box deletion (ΔTon) and the NTE deletion (ΔNTE), which are expressed at reasonable levels
286 (Fig. 4b). The ΔTon strain has a similar phenotype as ΔRagAB, demonstrating that this variant is
287 inactive and therefore that RagAB is a *bona-fide* TBDT. Strikingly, the ΔNTE variant resembles the
288 KRAB strain and does not grow even after a prolonged period (Fig. 4a). Since the ΔRagAB strain
289 (which also lacks the NTE) does grow after a lag phase, the results suggest that the NTE is
290 important. In Proteobacteria, structures of TBDTs with a different N-terminal domain (Pfam 07660;
291 STN) have been reported[28]. This domain interacts with an anti-sigma factor in the inner membrane
292 to stimulate TBDT expression in response to the presence of their cognate substrates, exemplified
293 by the *E. coli* FecA-FecIR system[29-31] in which the anti-sigma factor *fecR* and the sigma factor *fecI*
294 are located in the same operon as *fecA*. By contrast, while *P. gingivalis* has five anti-sigma factors,
295 none of these are located near the *ragAB* locus. Moreover, deletion of the N-terminal domain in
296 FecA only affects FecA upregulation and has no effect on transport activity[29], contrasting with the
297 dramatic phenotype for the RagA ΔNTE mutant. Thus, while an involvement of the RagA NTE in
298 signalling seems likely, establishing the signalling partner(s) and mechanism remains the subject
299 of further work.
300
301 **Peptide binding by RagAB is selective**
302 We next characterised peptide binding to RagAB in more detail. Since RagAB is purified with an
303 ensemble of peptides that cannot be removed without denaturing the complex, added peptides
304 compete with bound peptides, resulting in the measurement of apparent rather than true
305 dissociation constants. The 21-residue peptide KATAEALKKALEEAGAEVELK (henceforth named
306 P21; charge -1) from the C-terminus of ribosomal protein L7 was abundant in W83 KRAB RagAB
307 (Methods), and was synthesised in addition to its 12-residue core sequence (DKATAEALKKAL,
308 denoted P12; charge +1) that is also present in a number of similar peptides but, crucially, is not
309 identified as a RagAB-bound peptide. We also tested an 11-residue peptide (named P4; sequence
310 NIFKKNVGFKK) of the arginine deiminase ArcA from *Streptococcus cristatus* that was proposed to
311 bind to RagB from ATCC[32].
312
313 We used microscale thermophoresis (MST) to asses peptide binding to RagAB. Initially, we used
314 N-terminally fluorescein-labelled P4 peptide (P4-FAM) and unlabelled RagAB to maximise the
315 signal-to-noise, and obtained apparent dissociation constants of ~2 μM for W83 RagAB and ~0.2
316 μM for ATCC RagAB (Extended Data Fig. 7). The negative control Omp40-41 did not show
317 binding, demonstrating that these results are not due to non-specific partitioning of fluorescently-
318 labelled peptide into detergent micelles. However, the fluorophore may affect peptide binding in an
319 unpredictable way, and therefore we next performed MST experiments for unlabelled P21, P12

320 and P4 peptides and His-tag labelled RagAB from wild-type W83. Remarkably, we observed
321 robust binding only for P21, with an apparent K_d (~0.4 μM; Extended Data Fig. 7) similar to that
322 observed for substrate binding to classical TBDTs[33-34]. While the fit to a single binding site model is
323 reasonable, models that assume two binding sites yield significantly better fits (Supplementary Fig.
324 3). This provides an indication that the two $RagA_2B_2$ binding sites may not be equivalent, perhaps
325 due to cooperativity. The data for P12 and P4 suggest that these peptides cannot displace the
326 bound endogenous peptides. Notably, the result for unlabelled P4 contrasts with that for P4-FAM
327 (Discussion). We next asked whether the three peptides bind to RagB, purified from *E. coli*. W83
328 RagB produced good-quality binding curves with P21 and P4, with similar apparent dissociation
329 constants of ~2 mM, but no binding was observed for P12 (Extended Data Fig. 7). The relatively
330 low apparent affinities of RagB for oligopeptides are in good agreement with literature values for
331 oligosaccharide binding to SusD proteins determined via ITC[16,35,36]. Collectively, the P21 data
332 suggest that peptides bind with lower affinities to RagB (P21 K_d app. ~2 mM) than to RagAB (P21
333 K_d app. ~0.4 μM), which makes sense assuming that after initial capture by RagB, the peptide
334 needs to be transferred to RagA. The data also show that the P4 and P12 peptides are not good
335 substrates for W83 RagAB, confirming that the transporter has considerable substrate selectivity.
336
337 Since we can measure peptide binding to purified RagAB *in vitro* by MST, added peptides compete
338 successfully with co-purified endogenous peptides. This, together with the robust growth observed
339 in BSA-MM, led us to ask whether we could detect acquisition of BSA tryptic peptides by W83
340 RagAB *in vitro* (Methods). Indeed, the sample incubated with the BSA digest revealed six bound
341 BSA peptides in addition to endogenous peptides, suggesting that the BSA peptides only partly
342 replace the co-purified ensemble (Supplementary Table 2). This is due to the fact that the BSA
343 digest contains 63 different peptides, such that the concentration of BSA "binder" peptides is not
344 high enough to replace all endogenous peptides. By contrast, a 100-fold excess of P21 completely
345 displaced the co-purified peptides (Supplementary Table 2). The fact that only a subset of BSA
346 peptides binds to RagAB demonstrates that the transporter is selective. We also incubated the
347 BSA tryptic digest experiment with W83 RagB. Prior to incubation, RagB contains only one bound
348 co-purified peptide. After incubation and post-SEC, two BSA peptides are detected, demonstrating
349 that at least some peptides bind to RagB with sufficient affinity to survive SEC (Supplementary
350 Table 2).
351
352 In an attempt to build a unique peptide sequence into the electron density maps, we crystallised
353 RagAB purified from wild-type W83 in the absence and presence of a 50-fold molar excess of P21.
354 Comparison of the maps reveals peptide density at the same site, but with some differences
355 particularly at the N-terminus (Extended Data Fig. 8). However, the P21 sequence does not fit the
356 density unambiguously, and we therefore speculate that P21 and other peptides are bound with
357 register shifts and perhaps different chain directions. In all three structures the same RagAB

358 residues hydrogen bond with the backbones of the modelled substrates, providing a clear rationale
359 how the transporter can bind many oligopeptides. Future studies will be required to define
360 precisely how peptides bind to RagAB, perhaps by collecting anomalous X-ray data on P21-like
361 peptides labelled at unique positions with heavy atoms.
362

363 ## Discussion

364 Our combined data show that RagAB is a dynamic OM oligopeptide transporter that is important
365 for growth of *P. gingivalis* on extracellular protein substrates and possibly for peptide-mediated
366 signalling[32]. We propose a transport model in which the open RagB lid binds substrates before
367 delivering them to RagA via lid closure (Extended Data Fig. 9). This would make the RagA Ton box
368 accessible for interaction with TonB, permitting formation of a transport channel into the
369 periplasmic space. To test the premise that substrate binding induces lid closure we collected cryo-
370 EM data on RagAB in the absence and presence of excess P21. Particle classification indeed
371 shows a decrease in OO states and a clear increase in CC states in the P21 sample, in
372 accordance with our model (Extended Data Fig. 10).
373

374 How does signalling to TonB occur, and how are unproductive interactions of TonB with "empty"
375 transporters avoided? In the classical, smaller TBDTs such as FecA and BtuB, the ligand binding
376 sites involve residues of the plug domain, suggesting that ligand binding is allosterically
377 communicated to the periplasmic face of the plug. However, there are no direct interactions
378 between the visible, well-defined part of the peptide substrates and the RagA plug. What, then,
379 causes the observed conformational changes in the plug? One possibility is that parts of peptide
380 substrates that are invisible (*e.g.* due to mobility) contact the plug. Given the very large solvent-
381 excluded RagAB cavity even with the modelled 13-residue peptide (~ 9800 $Å^3$; ~11500 $Å^3$ without
382 peptide; Extended Data Fig. 3), there is enough space to accommodate the long substrates
383 identified by the peptidomics, and these could contact the plug directly. However, the presence of
384 substrate density in the open states of the cryo-EM structures suggests that it may not be the
385 occupation of the binding site *per se* that is important for TonB interaction, but closure of the RagB
386 lid (Extended Data Fig. 9). Thus, we hypothesise that certain peptides may bind to RagAB, but do
387 not generate the closed state of the complex and signal occupancy of the binding site to TonB.
388 This may provide an alternative explanation for the different MST results for the P4 and P4-FAM
389 peptide titrations to RagAB (Extended Data Fig. 7). Given the nature of the MST signal, titrating
390 unlabelled P4 to labelled RagAB is likely to give a signal only if the binding causes a
391 conformational change (*e.g.* lid closure in the case of RagAB). In the "reverse" experiment, the
392 readout is on the labelled peptide (P4-FAM), and the large change in mass upon binding could
393 generate a thermophoretic signal in the absence of any conformational change. Thus, P4 may be
394 an example of a substrate that binds non-productively to RagAB.
395

A fascinating question is why RagAB and related transporters are dimeric. To our knowledge, there are no other TBDTs that function as oligomers, and there is no obvious reason why dimerisation would be beneficial. There are few clues in the structures, but when RagA in, *e.g.*, the closed complexes of the CC and OC states is superposed, RagB shows a rigid-body shift of ~3-5 Å, and *vice versa*. A similar trend is observed when the open complexes of the OC and OO states are considered. Moreover, the peptide densities in the OO state are stronger than that of the open complex in the OC state (Fig. 3). Together, this suggests that the individual RagAB complexes could exhibit some kind of cross-talk such as cooperative substrate binding. This notion is supported by the MST data for P21 binding to RagAB, suggesting the presence of two, non-equivalent ligand binding sites.

Author contributions

MM, JP and BvdB initiated the project. MM cultured cells, purified and crystallised proteins and performed MST binding experiments, with guidance from JP and BvdB. JBRW and SR determined cryo-electron microscopy structures, supervised by NR. ZN performed cloning and strain construction. GB carried out qPCR experiments, and CS and JJE performed the peptidomics analysis. KP performed the MD simulations, supervised by UK. BvdB purified and crystallised proteins and determined the RagAB crystal structures. AB collected crystallography data. The manuscript was written by BvdB with input from MM, JBRW, NR and JP.

Acknowledgements

This work was supported by a Welcome Trust Investigator award (214222/Z/18/Z to BvdB). We would further like to thank personnel of the Diamond Light Source for beam time (Block Allocation Group numbers mx-13587 and mx-18598) and assistance with data collection. All EM was performed at the Astbury Biostructure Laboratory which was funded by the University of Leeds and the Wellcome Trust (108466/Z/15/Z). We thank Drs. Rebecca Thompson, Emma Hesketh and Dan Maskell for EM support. We would also like to thank T. Kantyka for help in designing MS experiments. This study was supported in part by National Science Centre, Poland grants UMO-2015/19/N/NZ1/00322 and UMO-2018/28/T/NZ1/00348 to MM, UMO-2016/23/N/NZ1/01513 to ZN, UMO-2018/29/N/NZ1/00992 to GPB, and UMO-2018/31/B/NZ1/03968 and NIDCR/DE 022597 (NIH) to JP. LC-MS/MS analysis was supported by the Novo Nordisk Foundation (BioMS). JBRW was supported by a Wellcome Trust 4 year PhD studentship (215064/Z/18/Z).

433 # Ethics declarations

434 **Competing interests**

435 The authors declare no competing interests.

436

437 # Methods

438 **Bacterial strains and general growth conditions.** *Porphyromonas gingivalis* strains (listed in
439 Table S4) were grown in enriched tryptic soy broth (eTSB per liter: 30 g tryptic soy broth, 5 g yeast
440 extract; further supplemented with 5 mg hemin; 0.25 g L-cysteine and 0.5 mg menadione) or on
441 eTSB blood agar (eTSB medium containing 1.5% [w:v] agar, further supplemented with 5%
442 defibrinated sheep blood) at 37 °C in an anaerobic chamber (Don Whitley Scientific, UK) with an
443 atmosphere of 90% nitrogen, 5% carbon dioxide and 5% hydrogen. *Escherichia coli* strains (listed
444 in Supplementary Table 4), used for all plasmid manipulations, were grown in Luria–Bertani (LB)
445 medium and on 1.5% agar LB plates. For antibiotic selection in *E. coli*, ampicillin was used at 100
446 µg/ml. *P. gingivalis* mutants were grown in the presence of erythromycin at 5 µg/ml and/or
447 tetracycline at 1 µg/ml.

448

449 **Growth of *P. gingivalis* in minimal medium supplemented with BSA.** An important general
450 limitation of studies on TonB-dependent transport is that it has not yet been reconstituted *in vitro*
451 from purified components, due to the involvement of two membranes, one of which has to be
452 energised and contain the ExbBD-TonB complex. This limits the ability to directly link any TBDT to
453 substrate import. Therefore, to determine the role of RagAB in the transport of peptides *in vivo*, a
454 growth assay with minimal medium containing BSA as the sole carbon source (BSA-MM) was
455 used. Notably, the peptides generated by extracellular *P. gingivalis* proteases such as gingipains
456 must be intracellular to allow growth, giving a qualitative measure of peptide import. *P. gingivalis*
457 strains were grown overnight in eTSB. The cultures were washed twice with enriched Dulbecco's
458 Modified Eagle's Medium (eDMEM per liter: 10 g BSA; further supplemented with 5 mg hemin;
459 0.25 g L-cysteine and 0.5 mg menadione) and finally resuspended in eDMEM. The OD600 in each
460 case was adjusted to 0.2 and bacteria were grown for 40 hours. OD600 was measured at 5 hour
461 intervals.

462

463 **Mutant construction.** For RagA, the following mutants were made: a Ton box deletion (ΔTon;
464 residues V100-Y109 deleted), a NTE domain deletion (ΔNTE; residues V25-K99 deleted) a
465 putatively monomeric RagAB version made via introduction of a His6-tag between residues Q570-
466 G571; $RagAB_{mono}$), and deletions of the two loops (L7 and L8) that remain associated with RagB
467 during lid opening as based on the cryo-EM structures (Δhinge1, residues Q670-G691 deleted and
468 replaced by one Gly; Δhinge2, residues L731-N748 deleted and replaced by one Gly). For RagB,
469 two variants were made, both involving the acidic loop: a deletion of this loop (Δ_{AL}; residues R97-

470 S104) and conversion of the acidic loop into a basic loop ($RagB_{BL}$; D99/E100/D101/E102 replaced
471 by R99/K100/R101/K102). All *P. gingivalis* mutants were prepared using wild-type W83 strain or its
472 derivatives (unless stated otherwise) and constructed by homologous recombination[37]. Mutants
473 were generated in wild type W83 rather than KRAB W83 due to the presence of multiple antibiotic
474 cassettes in the latter strain, resulting from removal of the gingipain genes. The "swap" mutants
475 were prepared using the ATCC33277 strain as background. For deletion strains, 1 kb regions
476 upstream (5') and downstream (3') from the *ragA*, *ragB* and both *ragAB* genes, as well as chosen
477 antibiotic resistance cassettes, were amplified by PCR. Obtained DNA fragments were cloned into
478 pUC19 vector using restriction digestion method and/or Gibson method[38]. For the construction of
479 master plasmids for RagA and RagB mutants the whole gene sequences were amplified with
480 addition of antibiotic cassettes, 1kb downstream fragments and cloned into pUC19 vector. Desired
481 mutations were introduced into master plasmids by SLIM PCR[39]. A similar method was used for
482 the "swap" RagB-W83inATCC and RagB-ATCCinW83 strains. In both deletion RagB plasmids we
483 inserted the gene of the other strain (i.e. *ragB* from W83 into ΔRagB-ATCC). We also obtained a
484 RagAB "swap" strains using the pTIO-1 plasmid[40]. The DNA sequences of *ragAB* from both strains
485 were cloned with the addition of their promoters into pTIO plasmids and further conjugated with the
486 opposite deletion strains using *E. coli* S-17 λpir (i.e. RagAB-W83-pTIO into delRagAB-ATCC)[41].
487 Primers used for plasmid construction and mutagenesis are listed in Supplementary Table 4. All
488 plasmids were analyzed by PCR and DNA sequencing. *P. gingivalis* competent cells[42] were
489 electroporated with chosen plasmids and plated on TSBY with appropriate antibiotics –
490 erythromycin (5 µg/ml) or tetracycline (1 µg/ml) and grown anaerobically for approximately 10
491 days. Clones were selected and checked for correct mutations by PCR and DNA sequencing.
492 Bacterial strains generated and used in this study are listed in Supplementary Table 4.
493
494 **W83 KRAB RagAB production and purification.** The non-His tagged RagAB complex from *P.*
495 *gingivalis* W83 KRAB was isolated from cells grown in rich media. In brief, cells from 6 l of culture
496 were lysed by 1 pass through a cell disrupter (0.75 kW; Constant Biosystems) at 23,000 psi,
497 followed by ultracentrifugation at 200,00 x g for 45 minutes to sediment the total membrane
498 fraction. The membranes were homogenised and pre-extracted with 100 ml 0.5% sarkosyl in 20
499 mM Hepes pH 7.5 (20 min gentle stirring at room temperature) followed by ultracentrifugation
500 (200,000 x g; 30 min) to remove inner membrane proteins[43]. The sarkosyl wash step was repeated
501 once, after which the pellet (enriched in OM proteins) was extracted with 100 ml 1% LDAO (in 10
502 mM Hepes/50 mM NaCl pH 7.5) for 1 hour by stirring at 4 °C. The extract was centrifuged for 30
503 min at 200,000 x g to remove insoluble debris. The solubilised OM was loaded on a 6 ml
504 Resource-Q column and eluted with a linear NaCl gradient to 0.5 M over 20 column volumes.
505 Fractions containing RagAB were ran on analytical SEC (Superdex 200 Increase GL 10/300) in 10
506 mM Hepes/100 mM NaCl/0.05% LDAO pH 7.5 in order to obtain RagAB of sufficient purity. Finally,

507 the protein was detergent-exchanged to C_8E_4 using two rounds of ultrafiltration (100 kDa MWCO),
508 concentrated to 15-20 mg/ml and flash-frozen in liquid nitrogen.
509
510 **Wild type W83 RagAB production and purification.** Homologous recombination was used to
511 add a 8×His-tag to the C terminus of genomic *ragB* in the *P. gingivalis* W83 strain. The mutant was
512 grown about 20 h in rich medium under anaerobic conditions. The cells from 6 l of culture were
513 collected and processed as outlined above. The insoluble material was homogenised with 1.5%
514 LDAO (in 20 mM Tris-HCl/300 mM NaCl pH 8.0) and the complex was purified by nickel-affinity
515 chromatography (Chelating Sepharose; GE Healthcare) followed by gel filtration using a HiLoad
516 16/60 Superdex 200 column in 10 mM Hepes/100 mM NaCl, 0.05% DDM pH 8.0.
517
518 **Purification of RagB from W83 and ATCC 33277 expressed in *E. coli*.** Genes encoding for the
519 mature parts of RagB from W83 and ATCC 33277 (with His6-tags at the C-terminus) were
520 amplified by PCR from genomic DNA extracted from *P. gingivalis*. The DNA fragments were
521 purified and cloned into the arabinose-inducible pB22 expression vector[44] using NcoI/XbaI
522 restriction enzymes. The obtained expression plasmid was transformed into *E. coli* strain BL21
523 (DE3). Transformed *E. coli* cells were grown in LB media containing ampicillin (100 µg/ml) at 37 °C
524 to an OD_{600} ~ 0.6 and expression of the recombinant protein was induced with 0.1% arabinose.
525 After ~2.5 h at 37 °C, cells were collected by centrifugation (5,000 × g; 15 min), resuspended in 20
526 mM Tris-HCl/300 mM NaCl pH 8.0 and lysed by 1 pass through a cell disrupter (0.75 kW; Constant
527 Biosystems) at 23,000 psi, followed by ultracentrifugation at 200,000 × g for 45 minutes. The
528 supernatant was loaded on nickel-affinity resin (Chelating Sepharose; GE Healthcare) and after
529 washing with 30 mM imidazole, protein was eluted with buffer containing 250 mM imidazole.
530 Protein was further purified by gel filtration in 10 mM Hepes/100 mM NaCl pH 7.5 using a HiLoad
531 16/60 Superdex 200 column.
532
533 **Crystallisation and structure determination of RagAB from W83 KRAB.** Sitting drop vapour
534 diffusion crystallisation trials were set up using a Mosquito crystallisation robot (TTP Labtech)
535 using commercially available crystallisation screens (MemGold 1 and 2; Molecular Dimensions).
536 Initial hits were optimised manually by hanging drop vapour diffusion. Crystals were cryoprotected
537 by transferring them for 5-10 s in mother liquor containing an additional 10% PEG400. A few
538 crystals optimised from MemGold 2 condition C8 (18% PEG200, 0.1 M KCl, 0.1 M K-phosphate pH
539 7.5) diffracted anisotropically to below 4 Å at the Diamond Light Source (DLS) synchrotron at
540 Didcot, UK (space group $C222_1$; cell dimensions ~190 x 377 x 369 Å, with four RagAB complexes
541 in the asymmetric unit). Data were processed via Xia2[45] or Dials[46]. The structure was solved by
542 molecular replacement with Phaser[47], using data to 3.4 Å resolution. The structures of RagB (PDB
543 5CX8) and a Sculptor-modified model of BT2264 SusC (PDB 5FQ8) were used as search models.
544 The RagAB model was built iteratively by a combination of manually building in COOT[48] and the

545 AUTOBUILD routine within Phenix[49], and was refined with Phenix[50] using TLS refinement with 1
546 group per chain. Given that the R values are reasonable and the R-R_{free} gaps are not excessively
547 large we did not use NCS in the final rounds of refinement. Using NCS also did not improve the
548 peptide density. The final R and R_{free} factors of the RagAB structure are 20.5 and 25.5%,
549 respectively (Supplementary Table 1). Structures of RagAB purified from wild type W83 (+/- P21)
550 were solved via molecular replacement using Phaser, using the best-defined RagAB complex as
551 search model. Structures were refined within Phenix as above (Supplementary Table 1) and
552 structure validation was carried out with MolProbity[51].
553
554 **Crystallisation and structure determination of wild type RagAB W83 in the absence and**
555 **presence of P21.** Crystallisation trials were performed as outlined above with the following
556 modifications: the protein was not detergent-exchanged after gel filtration in DDM; two other
557 commercially available crystallisation screens were used (MemChannel and MemTrans; Molecular
558 Dimensions); For co-crystallisation of RagAB W83 with P21 peptide, RagAB W83 at a
559 concentration of 17 mg/ml (~0.1 mM) was incubated overnight at 4 °C with 5 mM P21 peptide. For
560 RagAB W83 the crystals were optimised from MemTrans condition F6 (22% PEG400, 0.07 M
561 NaCl, 0.05 M Na-citrate pH 4.5), for RagAB W83 + P21 the crystals were optimised from
562 MemChannel condition D3 (15% PEG1000, 0.05 M Li-sulfate, 0.05 M Na-phosphate monobasic,
563 0.08 M citrate pH 4.5). Crystals were cryoprotected by transferring them for 5-10 s in mother liquor
564 containing additional PEG400 to generate a final concentration of ~25%.
565
566 **Microscale thermophoresis.** Initial isothermal titration calorimetry (ITC) experiments showed that
567 P4 addition to buffer without protein generated very large heats, precluding ITC as a method to
568 assess peptide binding. For MST, the Monolith NT.115 instrument (NanoTemper Technologies
569 GmbH, Munich, Germany) was used to analyse the binding interactions between P4, P12 and P21
570 peptides and RagAB from W83 as well as RagB from W83 and ATCC 33277. Proteins were
571 labelled with Monolith His-tag Labeling Kit RED-tris-NTA 2nd Generation (NanoTemper
572 Technologies). For all interactions the concentrations of both fluorescently labelled molecule and
573 ligand were empirically adjusted using Binding Check mode (MO.Control software, NanoTemper
574 Technologies). Experiments were performed in assay buffer (10 mM Hepes/100 mM NaCl pH 7.5)
575 with addition of 0.03% DDM in the case of RagABs. For the measurements, sixteen 1:1 ligand
576 dilutions were prepared and then mixed with one volume of labelled protein followed by loading
577 into Monolith NT.115 Capillaries. Initial fluorescence measurements followed by thermophoresis
578 measurement were carried out using 100% LED power and medium MST power, respectively.
579 Data for three independently pipetted measurements were analysed (MO.Affinity Analysis
580 software, NanoTemper Technologies), allowing for determination of apparent dissociation
581 constants (K_D app.). The data was presented using GraphPad Prism 8. The interactions between

582 unlabelled W83 and ATCC 33277 RagABs and FAM-labelled P4 peptide were determined in the
583 same way.
584
585 **Isolation of the outer membrane fractions for quantitation of RagAB.** Outer membrane
586 fractions from 1 l of culture were isolated using sarkosyl extraction method (see RagAB W83
587 KRAB production and purification). After extraction in LDAO, the samples in 10 mM Hepes/50 mM
588 NaCl pH 7.5 containing 1% LDAO were diluted 3 times and loaded on SDS-PAGE. The bands
589 were analysed quantitatively using Image Lab 6.0.1 software (BIO-RAD). The band at ~70 kDa
590 was used as a reference sample (loading control). This analysis allows comparison of the levels of
591 RagAB integrated into the OM and, in combination with the growth assays, a qualitative
592 assessment of function.
593
594 **Peptide identification by LC-MS.** Bound peptides were isolated by precipitation via addition of
595 trichloroacetic acid to a final concentration of 30% and incubation at 4 ºC for 2 hrs. Subsequently
596 the peptide-containing supernatants were collected by centrifugation at 17,000xg. The isolated
597 peptides were micropurified using Empore™ SPE Disks of C18 octadecyl packed in 10 µl pipette
598 tips.
599
600 LC-MS/MS was performed using an EASY-nLC 1000 system (Thermo Scientific) connected to a
601 QExactive+ Hybrid Quadrupole-Orbitrap Mass Spectrometer (Thermo Scientific). Peptides were
602 dissolved in 0.1 % formic acid and trapped on a 2 cm ReproSil-Pur C18-AQ column (100 µm inner
603 diameter, 3 µm resin; Dr. Maisch GmbH, Ammerbuch-Entringen, Germany). The peptides were
604 separated on a 15-cm analytical column (75 µm inner diameter) packed in-house in a pulled
605 emitter with ReproSil-Pur C18-AQ 3 µm resin (Dr. Maisch GmbH, Ammerbuch-Entringen,
606 Germany). Peptides were eluted using a flow rate of 250 nl/min and a 20-minute gradient from 5%
607 to 35% phase B (0.1% formic acid and 90% acetonitrile or 0.1 % formic acid, 90 % acetonitrile and
608 5% DMSO). The collected MS files were converted to Mascot generic format (MGF) using
609 Proteome Discoverer (Thermo Scientific).
610
611 The data were searched against the *P. gingivalis* proteome (UniRef at uniprot.org) or the Swiss-
612 prot database using a bovine taxonomy. Database searches were conducted on a local mascot
613 search engine. The following settings were used: MS error tolerance of 10 ppm, MS/MS error
614 tolerance of 0.1 Da, and either non-specific enzyme or trypsin. Based on chromatogram peak
615 heights and the number of MS/MS spectra observed for a particular peptide in the mass
616 spectrometry data, the 21-residue peptide KATAEALKKALEEAGAEVELK (henceforth named P21;
617 charge -1) from ribosomal protein L7 is very abundant in W83 KRAB RagAB.
618

619 **Generation of BSA tryptic mixture.** BSA was solubilized in 100 mM ammonium bicarbonate/8M
620 urea pH 8.0. DTT was added to a final concentration of 10 mM and the mixture was incubated for
621 60 min at RT. Protein was alkylated by addition of iodoacetamide to a final concentration of 30 mM
622 and incubation for 60 min at RT in the dark. Next, the concentration of DTT was adjusted to 35 mM
623 followed by dilution of the sample to 1 M urea. For cleavage, trypsin from bovine pancreas (Sigma)
624 was added at 1:25 (trypsin : BSA) mass ratio and the sample was incubated overnight at 37 ºC.
625 Digestion was stopped by acidifying the sample to pH < 2.5 with formic acid. Peptides were
626 purified using Peptide Desalting Spin Columns (Thermo Scientific) and dried using Speed Vacuum
627 Concentrator Savant SC210A (Thermo Scientific).
628
629 **Acquisition of BSA-derived peptides and P21 by RagAB and RagB *in vitro*.**
630 W83 RagAB and W83 RagB were incubated overnight at 4 °C with an ~100-fold molar excess of
631 tryptic BSA digest (see Generation of BSA tryptic mixture) or P21 peptide. The samples were then
632 ran on Superdex 200 Increase GL 10/300 in 10 mM Hepes/100 mM NaCl pH 7.5 with addition of
633 0.03% DDM for RagAB W83. Fractions containing protein were pooled, acidified by addition of
634 formic acid to a final concentration 0.1% and analysed by MS.
635
636 **qPCR.** Samples of 1 ml of bacterial cultures (OD_{600} = 1.0) were centrifuged (5,000 x g; 5 min) at 4
637 °C, pellets were resuspended in 1 ml Tri Reagent (Ambion), incubated at 60 °C for 20 minutes,
638 cooled to room temperature and total RNA was isolated according to manufacturer instructions.
639 Genomic DNA was removed from samples by digestion with DNAse I (Ambion); 2 µg of RNA was
640 incubated with 2 U of DNAse for 60 minutes at 37 °C. Following digestion, RNA was purified using
641 Tri Reagent. Reverse transcription of 50 ng of RNA was performed with High-Capacity cDNA
642 Reverse Transcription Kit (Life Technologies), and reaction mixture was then diluted 20 times.
643 Real-time PCR was done in 10 µl reaction volume, using KAPA SYBR FAST qPCR Master Mix
644 (Kapa Biosystems) with 2 µl of diluted reverse transcription mixture as template. Primers used are
645 listed in Table S4. Reaction conditions were 3 minutes at 95 °C, followed by 40 cycles of
646 denaturation for 3 seconds at 95 °C and annealing/extension for 20 seconds at 60 °C. The reaction
647 was carried out with a CFX96 thermal cycler (Bio-Rad), and data was analysed in Bio-Rad CFX
648 Manager software.
649
650 **CryoEM sample preparation and data collection.** A sample of purified RagAB solubilised in a
651 DDM-containing buffer (10 mM HEPES pH 7.5, 100 mM NaCl, 0.03 % DDM) was prepared at 1.75
652 mg/ml (principle dataset) or 3 mg/ml (P21 addition experiment). For the P21 addition experiment,
653 control and P21-doped grids (with 50-fold molar excess of P21 peptide) were prepared at the same
654 time from the same purified stock of RagAB for consistency. In all cases, a 3.5 µL aliquot was
655 applied to holey carbon grids (Quantifoil 300 mesh, R1.2/1.3), which had been glow discharged at
656 10 mA for 30 s before sample application. Blotting and plunge freezing were carried out using a

657 Vitrobot Mark IV (FEI) with chamber temperature set to 6 °C and 100 % relative humidity. A blot
658 force of 6 and a blot time of 6 s were used prior to vitrification in liquid nitrogen-cooled liquid
659 ethane.
660
661 Micrograph movies were collected on a Titan Krios microscope (Thermo Fisher) operating at 300
662 kV with a GIF energy filter (Gatan) and K2 summit direct electron detector (Gatan) operating in
663 counting mode. Data acquisition parameters for each data set can be found in Supplementary
664 Table 3.
665
666 **Image processing.** Image processing was carried out using RELION (v2.1 and v3.0)[52,53]. Drift
667 correction was performed using MotionCor2[54] and contrast transfer functions were estimated using
668 gCTF[55]. Micrographs with estimated resolutions poorer than 5 Å and defocus values >4 µm were
669 discarded using a python script[56]. For the principle RagAB dataset, particles were autopicked in
670 RELION using a gaussian blob with a peak value of 0.3. Control and experimental datasets for the
671 P21 addition experiment were autopicked using the 'general model' in crYOLO[57]. In both cases,
672 particles were extracted in 216 x 216 pixel boxes and subjected to several rounds of 2D
673 classification in RELION[52]. 3D starting models were generated *de novo* from the EM data by
674 stochastic gradient descent in RELION. Processing of RagAB control and P21-doped datasets was
675 only taken as far as 3D classification.
676
677 For the principle RagAB dataset, three conformational states representing the CC, OC and OO
678 states were apparent in the first round of 3D classification and the corresponding particle stacks
679 were treated independently in further processing. C2 symmetry was applied to both the CC and
680 OO reconstructions. Post-processing was performed using soft masks and yielded reconstructions
681 for the CC, OC and OO states with resolutions of 3.7 Å, 3.7 Å and 3.9 Å respectively, as estimated
682 by gold standard Fourier Shell Correlations using the 0.143 criterion. The original micrograph
683 movies were later motion corrected in RELION 3.0[53]. Particles contributing to the final
684 reconstructions were re-extracted from the resulting micrographs. Following reconstruction,
685 iterative rounds of per-particle CTF refinement, with beam tilt estimation, and Bayesian particle
686 polishing were employed which improved the resolution of post-processed CC, OC and OO maps
687 to 3.3 Å, 3.3 Å and 3.4 Å respectively.
688
689 **Model building into cryoEM maps.** Examination of the maps revealed that their handedness was
690 incorrect. Maps were therefore Z-flipped in UCSF Chimera[58]. The RagAB W83 KRAB crystal
691 structure was rigid-body fit to the CC density map and subjected to several iterations of manual
692 refinement in COOT and 'real space refinement' in Phenix[50]. The asymmetric unit was
693 symmetrised in Chimera after each iteration. Starting models for the OC and OO states of the
694 complex were obtained from the CC structure by rigid-body fitting of one or both RagB subunits to

their cognate open density in the OC and OO maps respectively. These too were subjected to several iterations of manual refinement in COOT and 'real space refinement' in Phenix. Molprobity was used for model validation[51].

Molecular Dynamics simulations. The bound peptide in the refined crystal structure of a RagAB "monomer" was removed *in silico* and the system was inserted into a palmitoyloleoyl-phosphatidylethanolamine (POPE) bilayer using the CHARMM-GUI Membrane Builder[59]. The systems were solvated using a TIP3P water box and neutralized by adding the required counter-ions. Simulations were performed using GROMACS 5.1.2[60] and the all-atom CHARMM36 force fields[61,62]. For the long-range Coulomb interactions, the partice-mesh Ewald (PME) summation method[63] has been employed with a short-range cutoff of 12 Å and a Fourier grid spacing of 0.12 nm. In addition, the Lennard-Jones interactions were considered up to a distance of 10 Å and a switch function was used to turn off interactions smoothly at 12 Å. Achieved by semi-isotropic coupling to a Parrinello-Rahman barostat[64] at 1 bar with a coupling constant of 5 ps, the final unbiased simulations were performed in the isothermal-isobaric (NPT) ensemble. A Nosé-Hoover thermostat[65,66] was used to keep the temperature at 300 K with a coupling constant of 1 ps. A total of three simulations of 2500 ns were carried out for the apo complex with a time step of 2 fs by applying constraints on hydrogen atom bonds using the LINCS algorithm[67]. Similarly, the dimeric complex of $RagA_2B_2$ in the OO state was simulated for 500 ns. Cavity calculations were performed using CASTp[68].

Data availability

The data supporting the findings of this study are available from the corresponding authors upon reasonable request. Coordinates and structure factors that support the findings of this study have been deposited in the Protein Data Bank with accession codes 6SLI (KRAB RagAB), 6SLJ (WT RagAB) and 6SLN (WT RagAB + P21). EM structure coordinates have been deposited in the Electron Microscopy Data Bank with accession codes 6SM3 (CC), 6SMQ (OC) and 6SML (OO). The raw cryoEM movie mode micrographs for the primary dataset containing the CC, OC and OO structures, will be deposited in the EMPIAR database. Source data for Figs. 1a, 4a-d and Extended Data Figs. 2, 6a,b and 7 are included in this article and its Supplementary Information files.

References

731 1. Socransky, S. S., Haffajee, A. D., Cugini, M. A., Smith, C. & Kent, R. L. Jr. Microbial
732 complexes in subgingival plaque. *J. Clin. Periodontol.* **25**, 134–44 (1998).
733 2. Eke, P. I. et al. Update on prevalence of periodontitis in adults in the United States:
734 NHANES 2009 to 2012. *J. Periodontol.* **86**, 611–22 (2015).
735 3. Dominy, S. S. et al. *Porphyromonas gingivalis* in Alzheimer's disease brains: evidence for
736 disease causation and treatment with small-molecule inhibitors. *Sci. Adv.* **5**, eaau3333
737 (2019).
738 4. Potempa, J., Mydel, P. & Koziel, J. The case for periodontitis in the pathogenesis of
739 rheumatoid arthritis. *Nat. Rev. Rheumatol.* **13**, 606–620 (2017).
740 5. Tonetti, M. S. et al. Treatment of periodontitis and endothelial function. *N. Engl. J. Med.*
741 **356**, 911–920 (2007).
742 6. Usher, A. K. & and Stockley, R. A. The link between chronic periodontitis and COPD: a
743 common role for the neutrophil? *BMC Med.* **11**, 241 (2013).
744 7. Bui, F. Q. et al. Association between periodontal pathogens and systemic disease. *Biomed*
745 *J.* **42**, 27-35 (2019).
746 8. Mayrand, D. & Holt, S. C. Biology of asaccharolytic black-pigmented *Bacteroides* species.
747 *Microbiol. Rev.* **52**, 134–152 (1988).
748 9. Nemoto, T. K., Ohara-Nemoto, Y., Bezerra, G. A., Shimoyama, Y. & Kimura, S. A.
749 *Porphyromonas gingivalis* periplasmic novel exopeptidase, acylpeptidyl oligopeptidase,
750 releases N-acylated di- and tripeptides from oligopeptides. *J. Biol. Chem.* **291**, 5913–5925
751 (2016).
752 10. Potempa, J., Banbula, A. & Travis, J. Role of bacterial proteinases in matrix destruction and
753 modulation of host responses. *Periodontol. 2000* **24**,153–192 (2000).
754 11. Grenier, D. et al. Role of gingipains in growth of *Porphyromonas gingivalis* in the presence
755 of human serum albumin. *Infect. Immun.* **69**, 5166–5172 (2001).
756 12. Nagano, K. et al. Characterization of RagA and RagB in *Porphyromonas gingivalis*: study
757 using gene-deletion mutants. *J. Med. Microbiol.* **56**, 1536–1548 (2007).
758 13. Goulas, T. et al. Structure of RagB, a major immunodominant outer-membrane surface
759 receptor antigen of *Porphyromonas gingivalis*. *Mol. Oral Microbiol.* **31**, 472–485 (2016).
760 14. Bolam, D. N. & van den Berg, B. TonB-dependent transport by the gut microbiota: novel
761 aspects of an old problem. *Curr. Opin. Struct. Biol.* **51**, 35–43 (2018).
762 15. Bolam, D. N. & Koropatkin, N. M. Glycan recognition by the Bacteroidetes Sus-like
763 systems. *Curr. Opin. Struct. Biol.* **22**, 563–569 (2012).
764 16. Glenwright, A. J. et al. Structural basis for nutrient acquisition by dominant members of the
765 human gut microbiota. *Nature* **541**, 407–411 (2017).
766 17. Krissinel, E. & Henrick, K. Inference of macromolecular assemblies from crystalline state. *J.*
767 *Mol. Biol.* **372**, 774–797 (2007).

768 18. Noinaj, N., Guillier, M., Barnard, T. J. & Buchanan, S. K. TonB-dependent transporters:
769 regulation, structure, and function. *Annu. Rev. Microbiol.* **64**, 43-60 (2010).
770 19. Freed, D. M., Horanyi, P. S., Wiener, M. C. & Cafiso, D. S. Conformational exchange in a
771 membrane transport protein is altered in protein crystals. *Biophys. J.* **99**, 604-10 (2010).
772 20. Hickman, S. J., Cooper, R. E. M., Bellucci, L., Paci, E. & Brockwell, D. J. Gating of TonB-
773 dependent transporters by substrate-specific forced remodelling. *Nat. Commun.* **8**, 14804
774 (2017).
775 21. Gómez-Santos, N., Glatter, T., Koebnik, R., Świątek-Połatyńska, M. A. & Søgaard-
776 Andersen, L. A. TonB-dependent transporter is required for secretion of protease PopC
777 across the bacterial outer membrane. *Nat. Commun.* **10**, 1360 (2019).
778 22. Hall, L. M. et al. Sequence diversity and antigenic variation at the rag locus of
779 *Porphyromonas gingivalis*. *Infect. Immun.* **73**, 4253–4262. (2005).
780 23. Milner, P., Batten, J. E. & Curtis M. A. Development of a simple chemically defined medium
781 for Porphyromonas gingivalis: requirement for alpha-ketoglutarate. *FEMS Microbiol. Lett.*
782 **140**, 125-30 (1996).
783 24. Grenier, D. et al. Role of gingipains in growth of Porphyromonas gingivalis in the presence
784 of human serum albumin. *Infect. Immun.* **69**, 5166-72 (2001).
785 25. Nagano, K. et al. Trimeric structure of major outer membrane proteins homologous to
786 OmpA in Porphyromonas gingivalis. *J. Bacteriol.* **187**, 902-11 (2005).
787 26. Lamster, I. B. & and Ahlo, J. K. Analysis of gingival crevicular fluid as applied to the
788 diagnosis of oral and systemic diseases. *Ann. N. Y. Acad. Sci.* **1098**, 216–29 (2007).
789 27. Curtis, M. A., Hanley, S. A. & Aduse-Opoku, J. The rag locus of *Porphyromonas gingivalis*:
790 a novel pathogenicity island. *J. Periodontal Res.* **34**, 400–405 (1999).
791 28. Josts, I., Veith, K. & Tidow, H. Ternary structure of the outer membrane transporter FoxA
792 with resolved signalling domain provides insights into TonB-mediated siderophore uptake.
793 *Elife* **8**, pii: e48528 (2019).
794 29. Kim, I., Stiefel, A., Plantör, S., Angerer, A. & Braun, V. Transcription induction of the ferric
795 citrate transport genes via the N-terminus of the FecA outer membrane protein, the Ton
796 system and the electrochemical potential of the cytoplasmic membrane. *Mol. Microbiol.* **23**,
797 333-44 (1997).
798 30. Braun, V., Mahren, S. & Ogierman, M. Regulation of the FecI-type ECF sigma factor by
799 transmembrane signalling. *Curr. Opin. Microbiol.* **6**, 173-80 (2003).
800 31. Koebnik R. TonB-dependent trans-envelope signalling: the exception or the rule? *Trends*
801 *Microbiol.* **13**, 343-7 (2005).
802 32. Ho, M. H., Lamont, R. J. & Xie, H. Identification of *Streptococcus cristatus* peptides that
803 repress expression of virulence genes in *Porphyromonas gingivalis*. *Sci. Rep.* **7**, 1413
804 (2017).

805 33. Moynié, L. et al. The complex of ferric-enterobactin with its transporter from Pseudomonas
806 aeruginosa suggests a two-site model. *Nat. Commun*. **10**, 3673 (2019).
807 34. Balhesteros, H. et al. TonB-Dependent Heme/Hemoglobin Utilization by Caulobacter
808 crescentus HutA. *J. Bacteriol*. **199**, e00723-16 (2017).
809 35. Koropatkin, N. M., Martens, E. C., Gordon, J. I. & Smith, T. J. Starch catabolism by a
810 prominent human gut symbiont is directed by the recognition of amylose helices. *Structure*
811 **16**, 1105-15 (2008).
812 36. Rogowski, A., et al. Glycan complexity dictates microbial resource allocation in the large
813 intestine. *Nat Commun*. **6**, 7481 (2015).
814 37. Nguyen, K. A., Travis, J. & Potempa, J. Does the importance of the C-terminal residues in
815 the maturation of RgpB from *Porphyromonas gingivalis* reveal a novel mechanism for
816 protein export in a subgroup of Gram-Negative bacteria? *J. Bacteriol.* **189**, 833–843 (2007)
817 38. Gibson, D. G. et al. Enzymatic assembly of DNA molecules up to several hundred
818 kilobases. *Nat. Methods* **6**, 343–345 (2009).
819 39. Chiu, J., March, P. E., Lee, R. & Tillett, D. Site-directed, Ligase-Independent Mutagenesis
820 (SLIM): a single-tube methodology approaching 100% efficiency in 4 h. *Nucleic Acids Res.*
821 **32**, e174 (2004).
822 40. Tagawa, J. et al. Development of a novel plasmid vector pTIO-1 adapted for
823 electrotransformation of *Porphyromonas gingivalis*. *J. Microbiol. Methods.* **105**, 174–179
824 (2014).
825 41. Belanger, M., Rodrigues, P. & Progulske-Fox, A. Genetic manipulation of *Porphyromonas*
826 *gingivalis. Curr. Protoc. Microbiol.* **5**, 13C.2.1–13C.2.24 (2007).
827 42. Smith, C. J. Genetic transformation of *Bacteroides* spp. using electroporation. *Methods Mol.*
828 *Biol.* **47**, 161–169 (1995).
829 43. Filip, C., Fletcher, G., Wulff, J. L. & Earhart, C. F. Solubilization of the cytoplasmic
830 membrane of *Escherichia coli* by the ionic detergent sodium-lauryl sarcosinate. *J. Bacteriol.*
831 **115**, 717–722 (1973).
832 44. Guzman, L. M., Belin, D., Carson, M. J. & Beckwith, J. Tight regulation, modulation, and
833 high-level expression by vectors containing the arabinose PBAD promoter. *J Bacteriol.* **177**,
834 4121–4130 (1995).
835 45. Winter, G., Lobley, C. M. & Prince, S. M. Decision making in xia2. *Acta Crystallogr. D Biol.*
836 *Crystallogr.* **69**, 1260–73 (2013).
837 46. Winter, G. et al. DIALS: implementation and evaluation of a new integration package. *Acta*
838 *Crystallogr. D Struct. Biol.* **74**, 85–97 (2018).
839 47. McCoy, A. J. et al. Phaser crystallographic software. *J. Appl. Crystallogr.* **40**, 658–674
840 (2007).
841 48. Emsley, P. & Cowtan, K. Coot: model-building tools for molecular graphics. *Acta*
842 *Crystallogr. D Biol. Crystallogr.* **60**, 2126–2132 (2004).

843 49. Afonine, P. V. et al. Towards automated crystallographic structure refinement with
844 phenix.refine. *Acta Crystallogr. D Biol. Crystallogr.* **68**, 352–367 (2012).
845 50. Adams, P. D. et al. PHENIX: a comprehensive Python-based system for macromolecular
846 structure solution. *Acta Crystallogr. D Biol. Crystallogr.* **66**, 213–221 (2010).
847 51. Chen, V. B. et al. MolProbity: all-atom structure validation for macromolecular
848 crystallography. *Acta Crystallogr. D Biol. Crystallogr.* **66**, 12–21 (2010).
849 52. Scheres, S. H. W. RELION: implementation of a Bayesian approach to cryo-EM structure
850 determination. *J. Struct. Biol.* **180**, 519–530 (2012).
851 53. Zivanov, J. et al. New tools for automated high-resolution cryo-EM structure determination
852 in RELION-3. *Elife* **7**, e42166 (2018).
853 54. Li, X., Zheng, S. Q., Egami, K., Agard, D. A. & Cheng, Y. Influence of electron dose rate on
854 electron counting images recorded with the K2 camera. *J. Struct. Biol.* **184**, 251–260
855 (2013).
856 55. Zhang, K. Gctf: Real-time CTF determination and correction. *J. Struct. Biol.* **193**, 1–12
857 (2016).
858 56. Thompson, R. F., Iadanza, M. G., Hesketh, E. L., Rawson, S. & Ranson, N. A. Collection,
859 pre-processing and on-the-fly analysis of data for high-resolution, single-particle cryo-
860 electron microscopy. *Nat. Protoc.* **14**, 100–118 (2019).
861 57. Wagner T. et al. SPHIRE-crYOLO is a fast and accurate fully automated particle picker for
862 cryo-EM. *Commun. Biol.* **2**, 218 (2019).
863 58. Petterson, E. F. et al. USCF Chimera – A visualization system for exploratory research and
864 analysis. *J. Comput. Chem.* **25**, 1605-1612. (2004).
865 59. Jo, S., Kim, T., Iyer, V. G. & Im, W. CHARMM-GUI: a web-based graphical user interface
866 for CHARMM. *J. Comput. Chem.* **29**, 1859–1865 (2008).
867 60. Abraham, M. J. et al. GROMACS: high performance molecular simulations through multi-
868 level parallelism from laptops to supercomputers. *SoftwareX.* **1**, 19–25 (2015).
869 61. Best, R. B. et al. Optimization of the additive CHARMM all-atom protein force field targeting
870 improved sampling of the backbone phi, psi and side-chain chi1 and chi2 dihedral angles.
871 *J. Chem. Theory Comput.* **8**, 3257–3273 (2012).
872 62. Klauda, J. B. et al. Update of the CHARMM all-atom additive force field for lipids: validation
873 on six lipid types. *J. Phys. Chem. B.* **114**, 7830–7843 (2010).
874 63. Darden, T., York, D. & Pedersen, L. Particle mesh ewald: an N log (N) method for ewald
875 sums in large systems. *J. Chem. Phys.* **98**, 10089–10092 (1993).
876 64. Parrinello, M. & Rahman, A. Polymorphic transitions in single crystals: a new molecular
877 dynamics method. *J. Appl. Phys.* **52**, 7182–7190 (1981).
878 65. Nosé, S. A. Molecular Dynamics Method for Simulations in the Canonical Ensemble. *Mol.*
879 *Phys.* **52**, 255−268 (1984).

66. Hoover, W. G. Canonical dynamics: equilibrium phase-space distributions. *Phys. Rev. A.* **31**, 1695 (1985).
67. Hess, B., Bekker, H., Berendsen, H. J. C. & Fraaije, J. G. E. M. LINCS: A linear constraint solver for molecular simulations. *J. Comput. Chem.* **18**, 1463–1472. (1997).
68. Tian, W., Chen, C., Lei, X., Zhao, J. & Liang, J. CASTp 3.0: computed atlas of surface topography of proteins. *Nucleic Acids Res.* **46**, W363–W367 (2018).
69. Schrödinger, L. L. C. The PyMOL Molecular Graphics System, Version 1.8.

Figure legends

Figure 1 Crystal structure of the RagA$_2$B$_2$ transporter suggests bound peptides. **a**, SDS-PAGE gel showing purified RagAB from W83 KRAB before (left lane) and after boiling in SDS-PAGE sample buffer. The gel is representative of three independent purifications. **b,c,** Views of RagA$_2$B$_2$ from the plane of the OM (**b**) and from the extracellular space (**c**). **d**, Side views of RagAB (right panel; surface representation) showing the bound peptide as a red space filling model. The plug domain of the RagA TBDT (cyan) is dark blue. **e**, 2Fo-Fc density (blue mesh; 1.0 σ, carve = 1.8) of the peptide after final refinement (left panel). The right panel shows potential hydrogen bonds (distance < 3.6 Å) between RagAB and the peptide backbone. Arbitrary peptide residue

914 numbering is indicated in italics. **f**, Extracellular views of RagAB with (left panel) and without the
915 RagB lid (green). **g**, Side view (top panel) and close-up of the RagB acidic loop (blue) and the
916 bound peptide. Potential hydrogen bonds are indicated by dashed lines. Structural figures were
917 made with Pymol[69].
918
919 **Figure 2 Different conformations of the $RagA_2B_2$ transporter revealed by cryo-EM**. **a-c**,
920 Cartoon views for closed-closed $RagA_2B_2$ (CC; **a**), open-closed (OC; **b**) and open-open (OO; **c**).
921 Views are from the plane of the OM (left and middle panels) and from the extracellular space (right
922 panel). Bound peptide is shown as space filling models in magenta. The plug domains of RagA are
923 coloured dark blue.
924
925 **Figure 3 Peptide and plug dynamics in $RagA_2B_2$ revealed via cryo-EM**. **a**, Density maps
926 viewed from the membrane plane of the closed-closed, open-closed and open-open $RagA_2B_2$
927 complexes coloured as in Figure 2. **b, c**. Isolated density for the plug domain and the bound
928 peptide ensemble viewed as in (**a**) and after a 90 degree clockwise rotation (**c)**. Additional density
929 for the plug domains of open RagAB complexes is shown in green. **d,e**, Superposition of RagA
930 plug domains in the open (yellow) and closed (cyan) RagAB complexes of the OC state, showing
931 different dynamics (**d;** view approximately as in **c**) and conformational changes (**e**) in going from
932 the open to the closed state. The Ton box region Q103-G108, visible only in the open state, is
933 coloured black with electron density shown in (**d**). In **e**, density for open and closed complexes is
934 shown for the region I214-R218.
935
936 **Figure 4 RagAB is important for growth on BSA. a**, Representative growth curves (n = 3, mean
937 ± standard error of the mean) for different *P. gingivalis* W83 and ATCC strains and mutant W83
938 *ragAB* variants on BSA-MM. **b**, Outer membrane RagAB protein expression levels for strains and
939 mutants determined by SDS-PAGE densitometry. **c**, Representative growth curves (n = 3, mean ±
940 standard error of the mean) for growth on BSA-MM for wild type *P. gingivalis* W83 and ATCC and
941 strains in which RagAB or RagB from ATCC was replaced with the corresponding ortholog from
942 W83. **d**, Corresponding OM protein expression levels of RagAB. Graphs in **b** and **d** show the mean
943 of two independent replicates. The dots show the individual replicates.

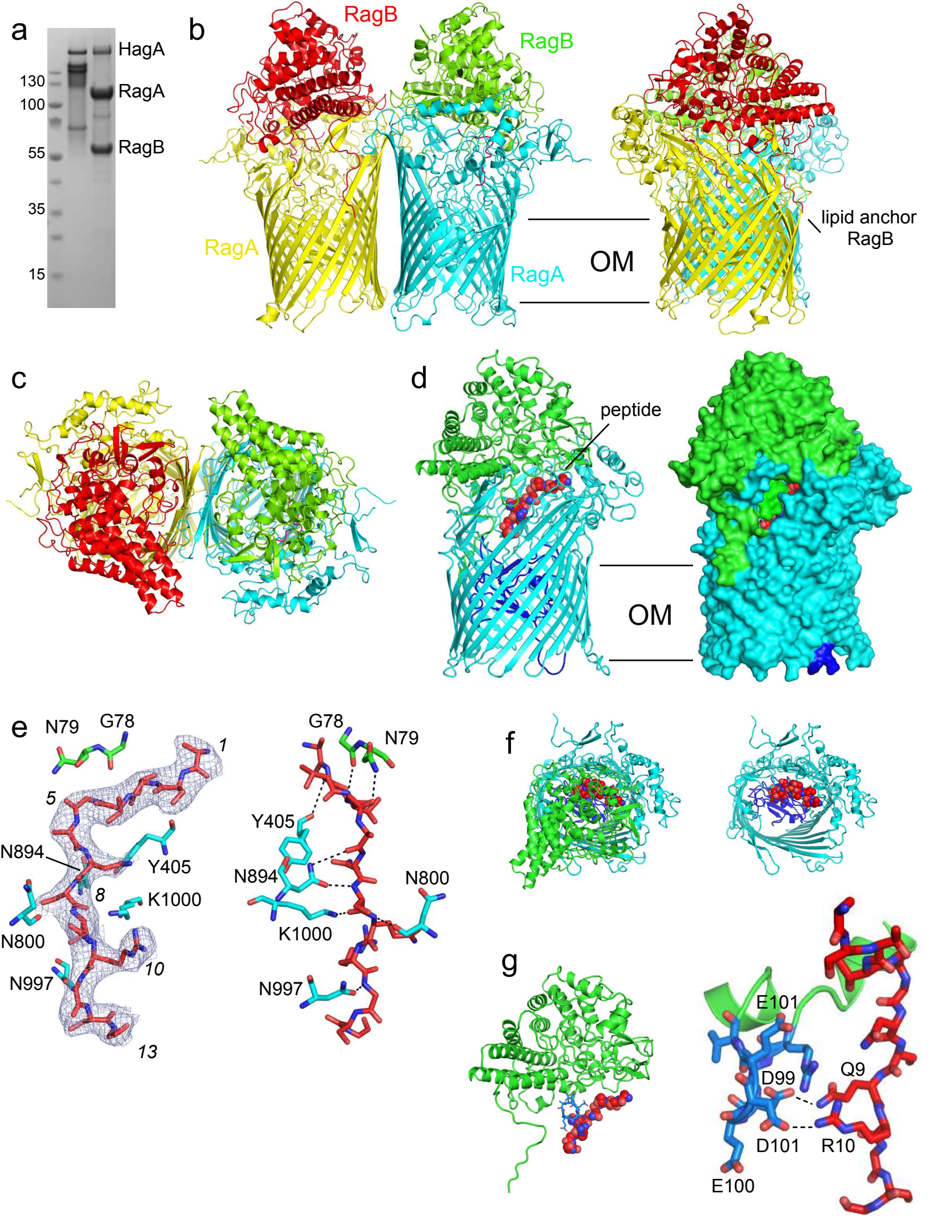
a
HagA
RagA
RagB
130
100
55
35
15
b
RagB
RagB
RagA
RagA
OM
lipid anchor
RagB
c
d
peptide
OM
e
N79
G78
1
5
N894
Y405
8
K1000
N800
10
N997
13
G78
N79
Y405
N894
N800
K1000
N997
f
g
E101
D99
Q9
D101
R10
E100

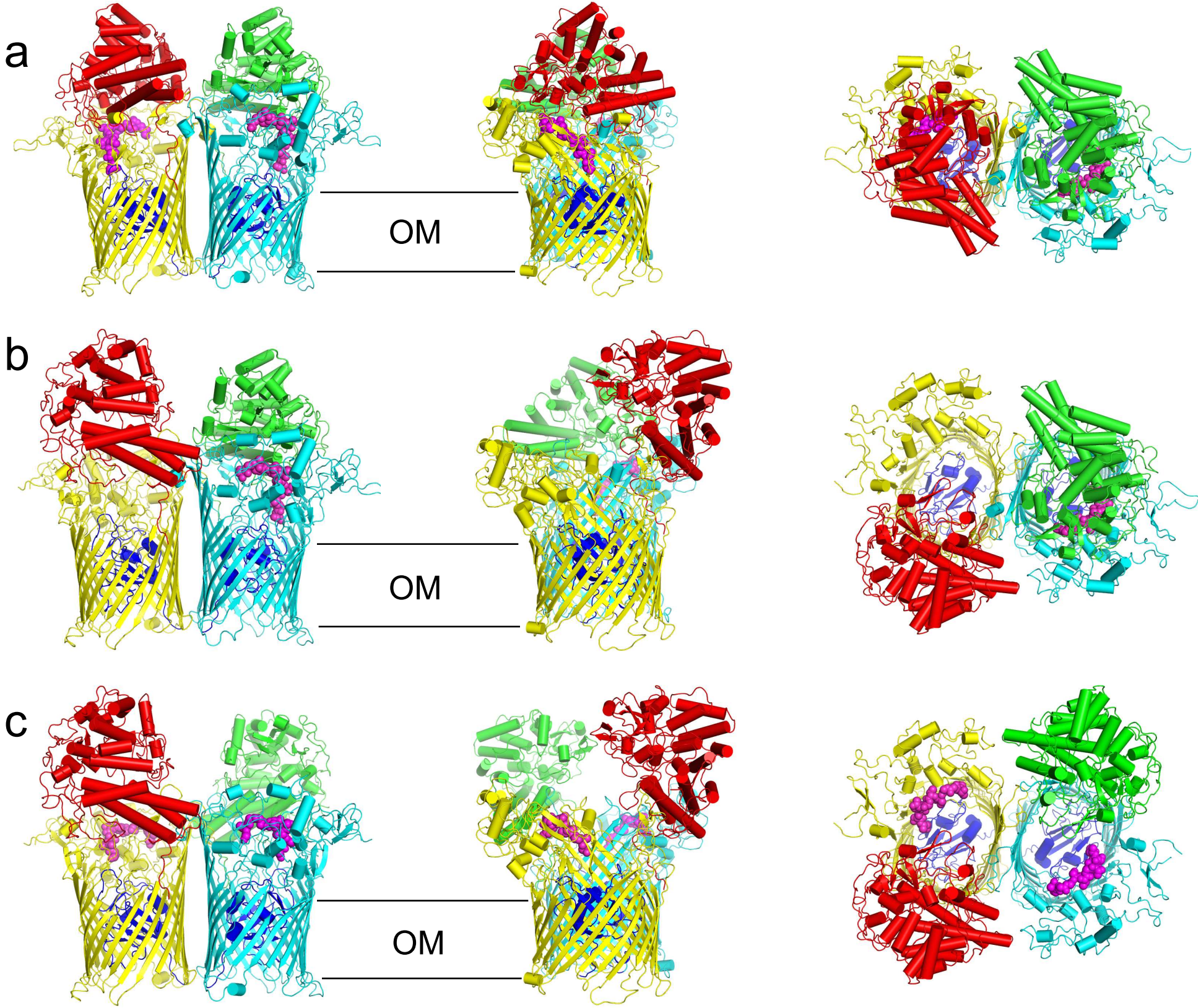
a
OM
b
OM
c
OM

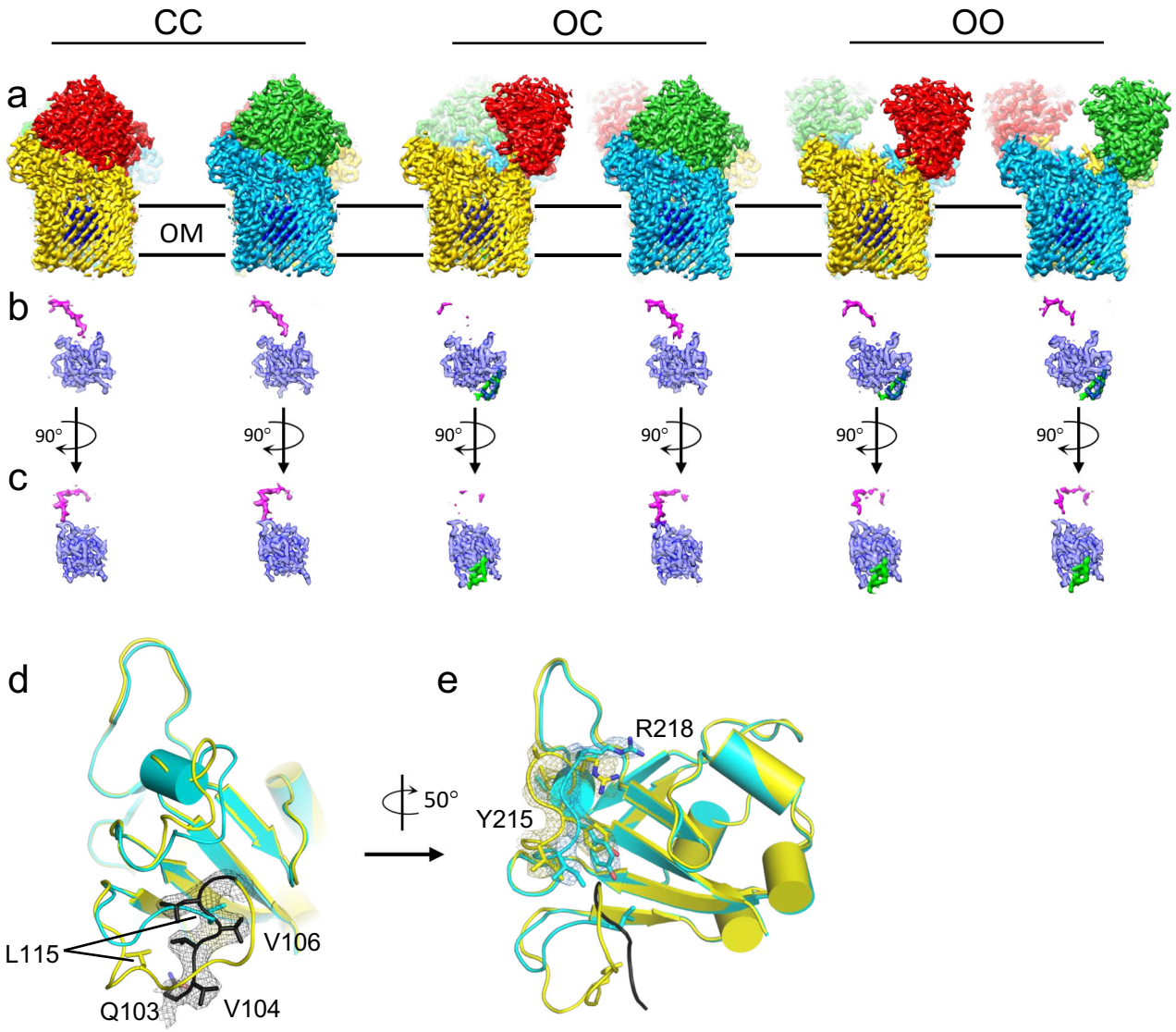
CC
OC
OO
a
OM
b
90°
c
d
e
50°
R218
Y215
L115
V106
Q103
V104

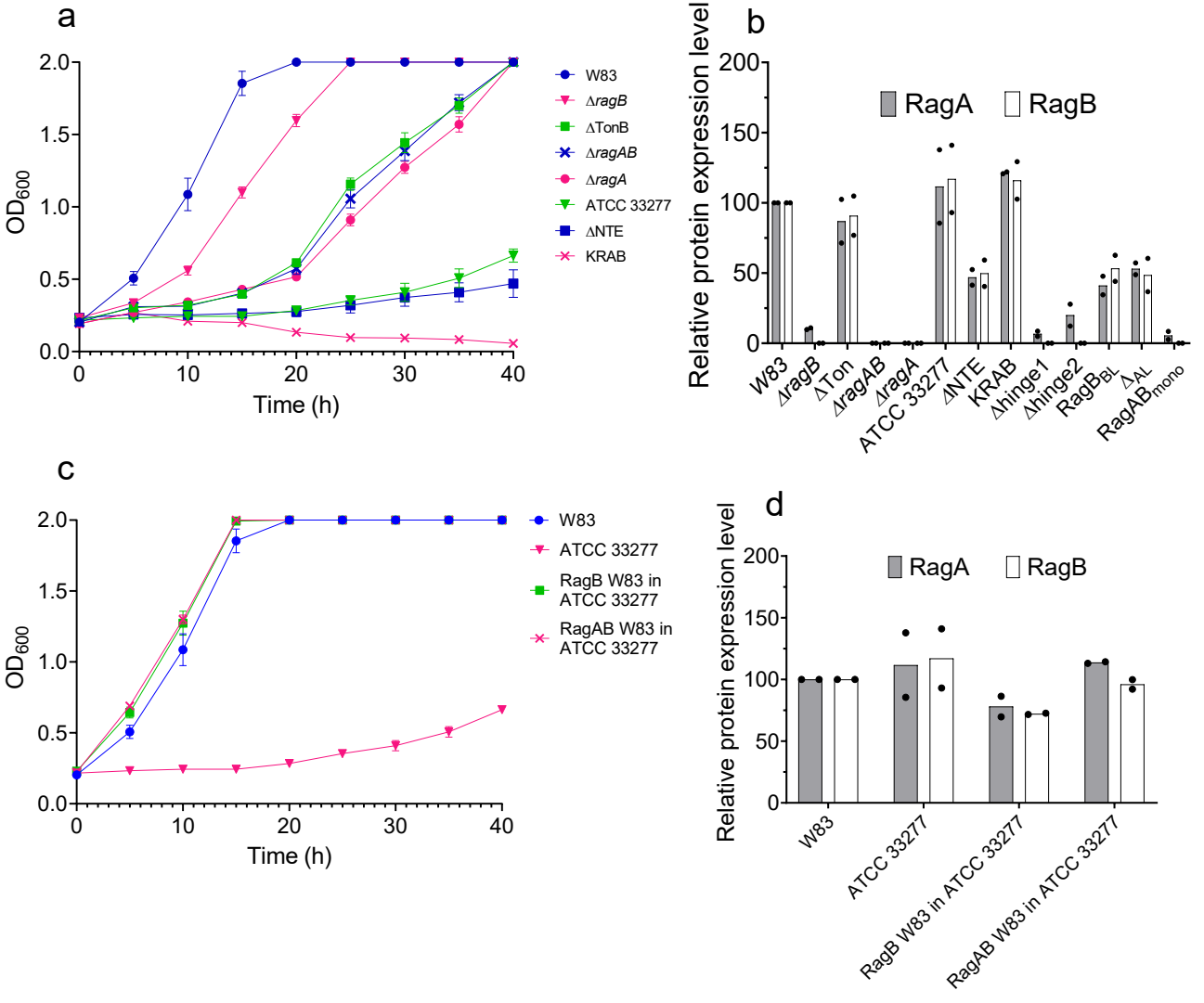
a
OD600
Time (h)
W83
ΔragB
ΔTonB
ΔragAB
ΔragA
ATCC 33277
ΔNTE
KRAB
b
Relative protein expression level
RagA
RagB
W83
ΔragB
ΔTon
ΔragAB
ΔragA
ATCC 33277
ΔNTE
KRAB
Δhinge1
Δhinge2
RagBBL
ΔAL
RagABmono
c
OD600
Time (h)
W83
ATCC 33277
RagB W83 in ATCC 33277
RagAB W83 in ATCC 33277
d
Relative protein expression level
RagA
RagB
W83
ATCC 33277
RagB W83 in ATCC 33277
RagAB W83 in ATCC 33277

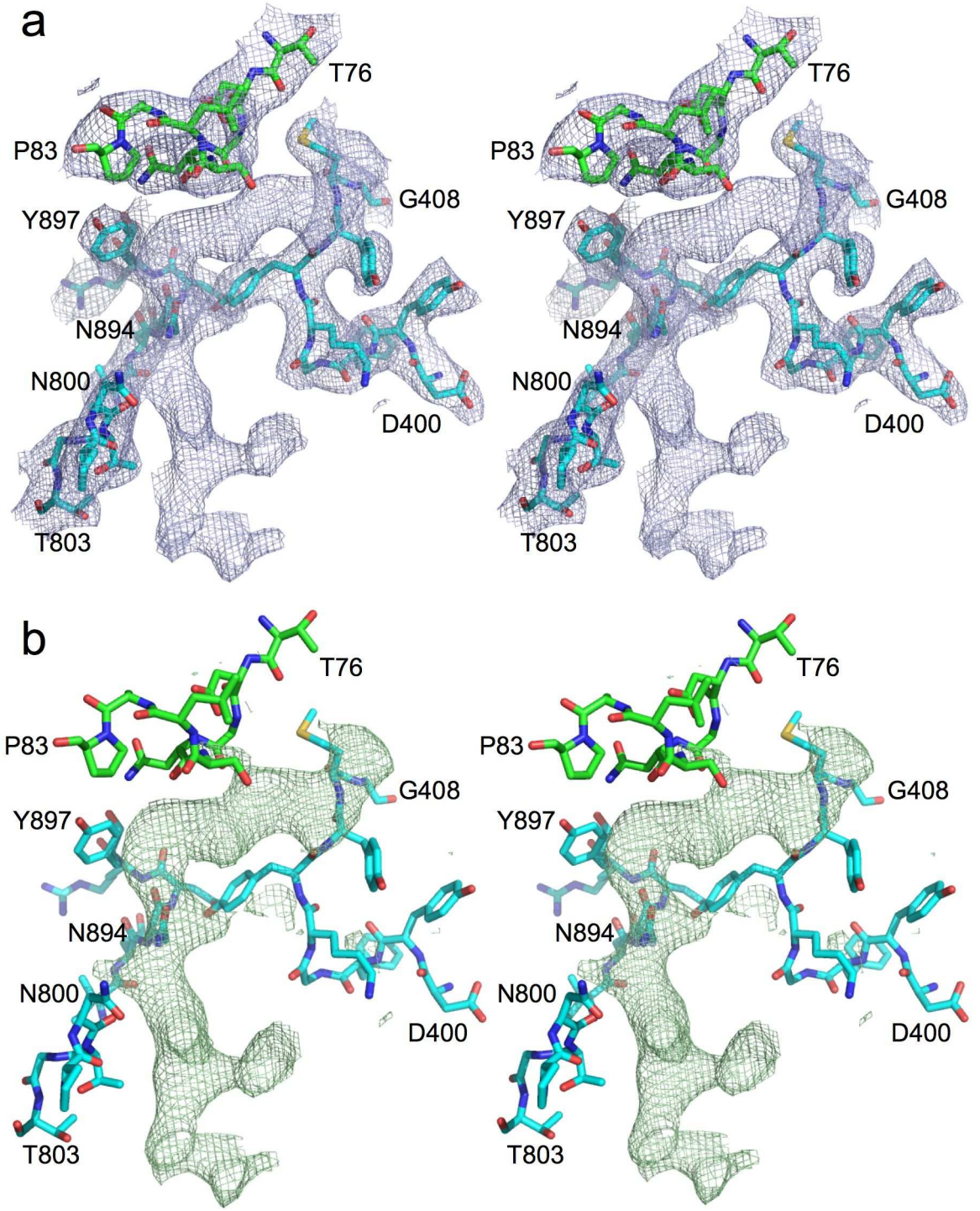
a
T76
P83
G408
Y897
N894
N800
D400
T803
T76
P83
G408
Y897
N894
N800
D400
T803
b
T76
P83
G408
Y897
N894
N800
D400
T803
T76
P83
G408
Y897
N894
N800
D400
T803

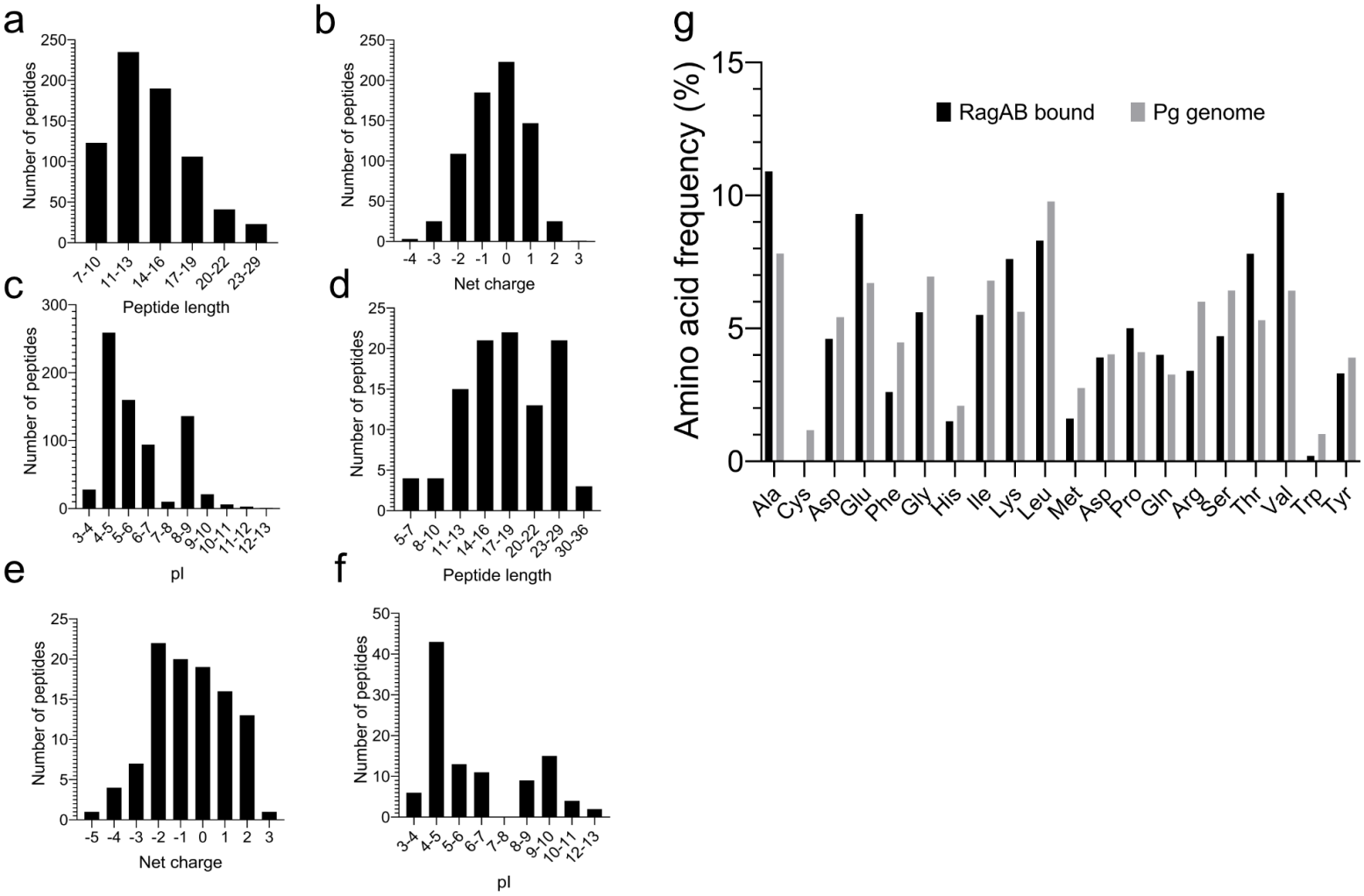
a
Number of peptides
250
200
150
100
50
0
7-10
11-13
14-16
17-19
20-22
23-29
Peptide length
b
Number of peptides
250
200
150
100
50
0
-4
-3
-2
-1
0
1
2
3
Net charge
c
Number of peptides
300
200
100
0
3-4
4-5
5-6
6-7
7-8
8-9
9-10
10-11
11-12
12-13
pI
d
Number of peptides
25
20
15
10
5
0
5-7
8-10
11-13
14-16
17-19
20-22
23-29
30-36
Peptide length
e
Number of peptides
25
20
15
10
5
0
-5
-4
-3
-2
-1
0
1
2
3
Net charge
f
Number of peptides
50
40
30
20
10
0
3-4
4-5
5-6
6-7
7-8
8-9
9-10
10-11
12-13
pI
g
Amino acid frequency (%)
15
10
5
0
RagAB bound
Pg genome
Ala
Cys
Asp
Glu
Phe
Gly
His
Ile
Lys
Leu
Met
Asp
Pro
Gln
Arg
Ser
Thr
Val
Trp
Tyr

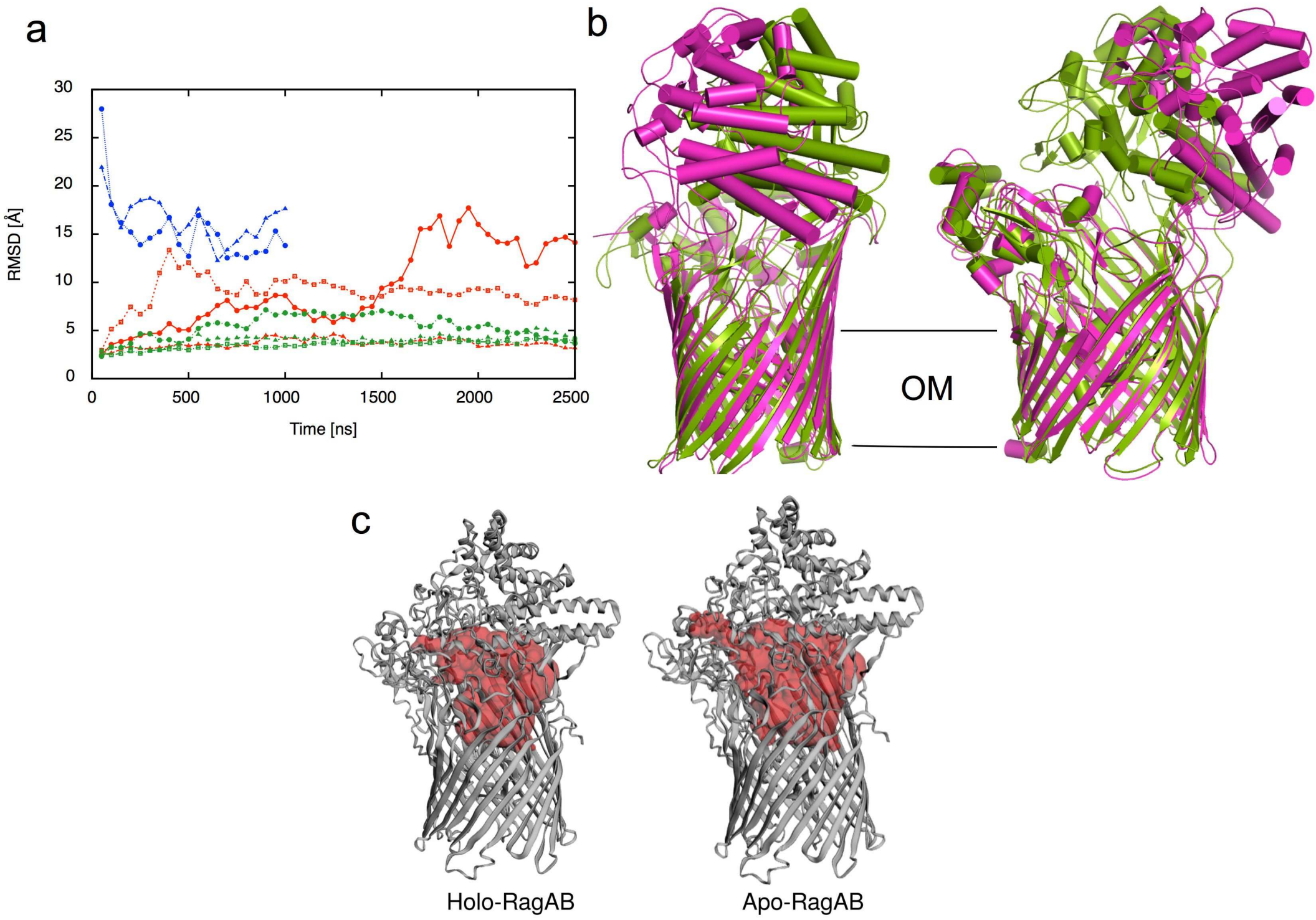
a
RMSD [Å]
Time [ns]
0
5
10
15
20
25
30
0
500
1000
1500
2000
2500
b
OM
c
Holo-RagAB
Apo-RagAB

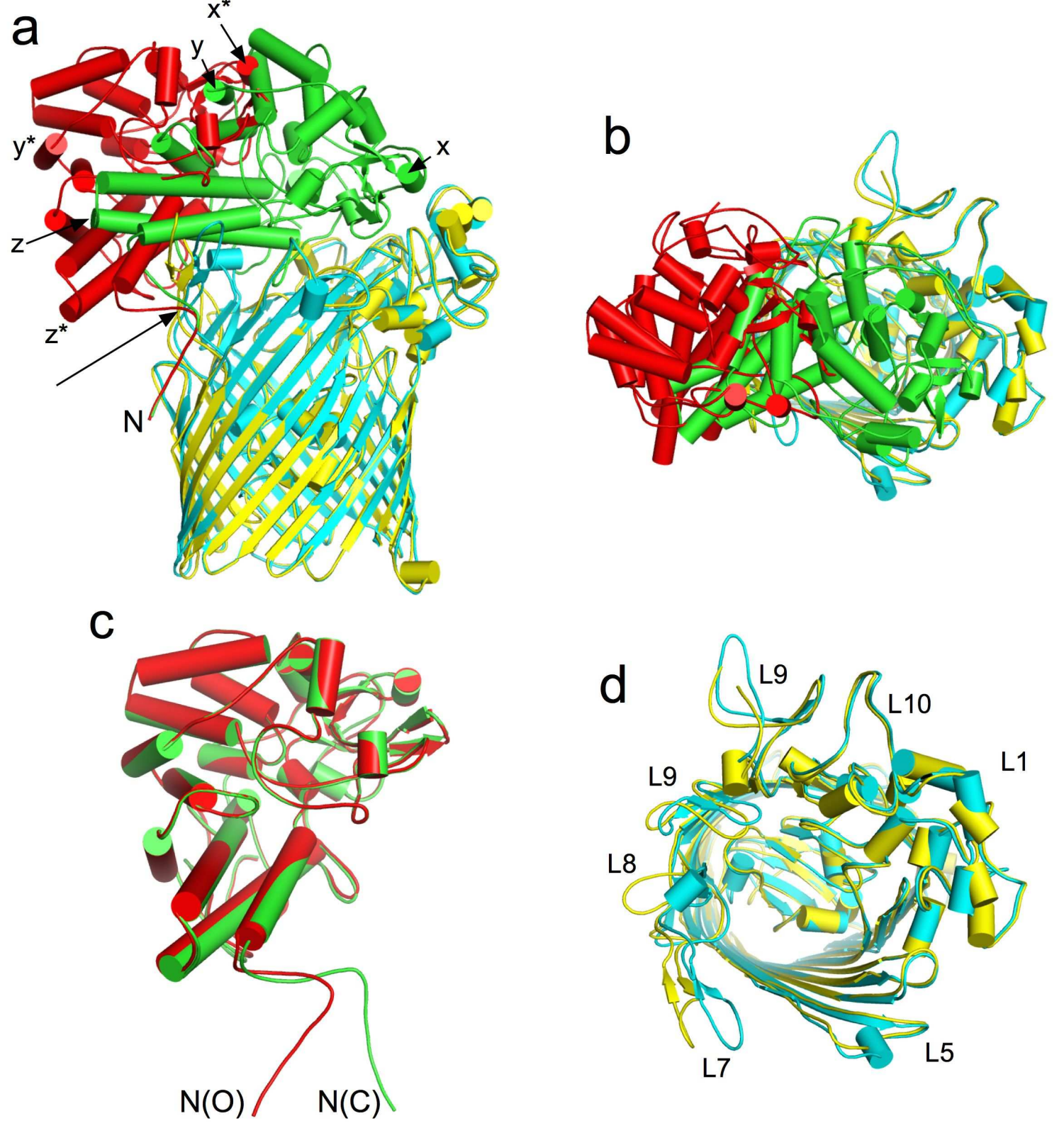
a
x*
y
y*
x
z
z*
N
b
c
N(O)
N(C)
d
L9
L10
L1
L9
L8
L7
L5

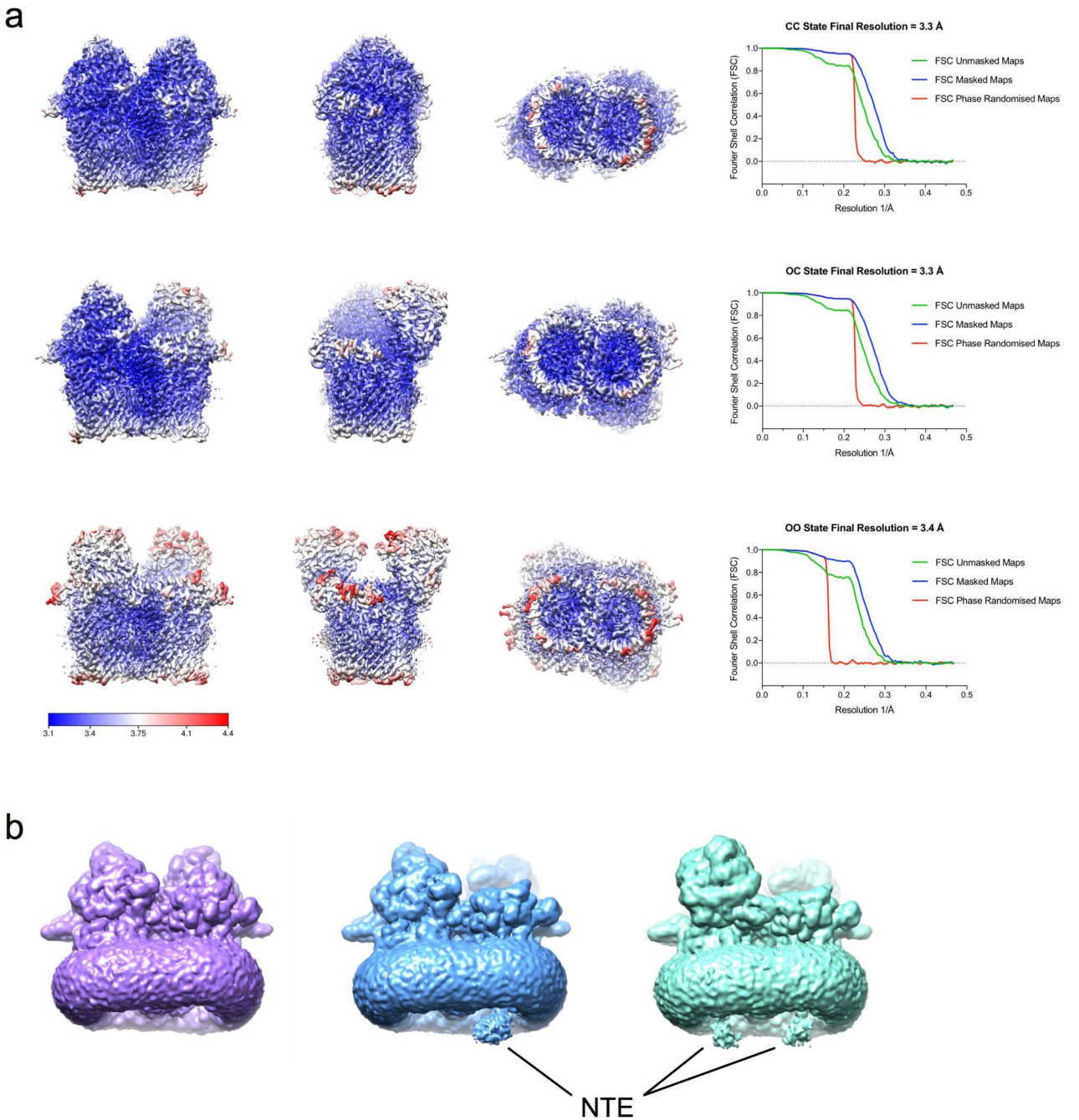
a
CC State Final Resolution = 3.3 Å
OC State Final Resolution = 3.3 Å
OO State Final Resolution = 3.4 Å
FSC Unmasked Maps
FSC Masked Maps
FSC Phase Randomised Maps
Fourier Shell Correlation (FSC)
Resolution 1/Å
3.1
3.4
3.75
4.1
4.4
b
NTE

a

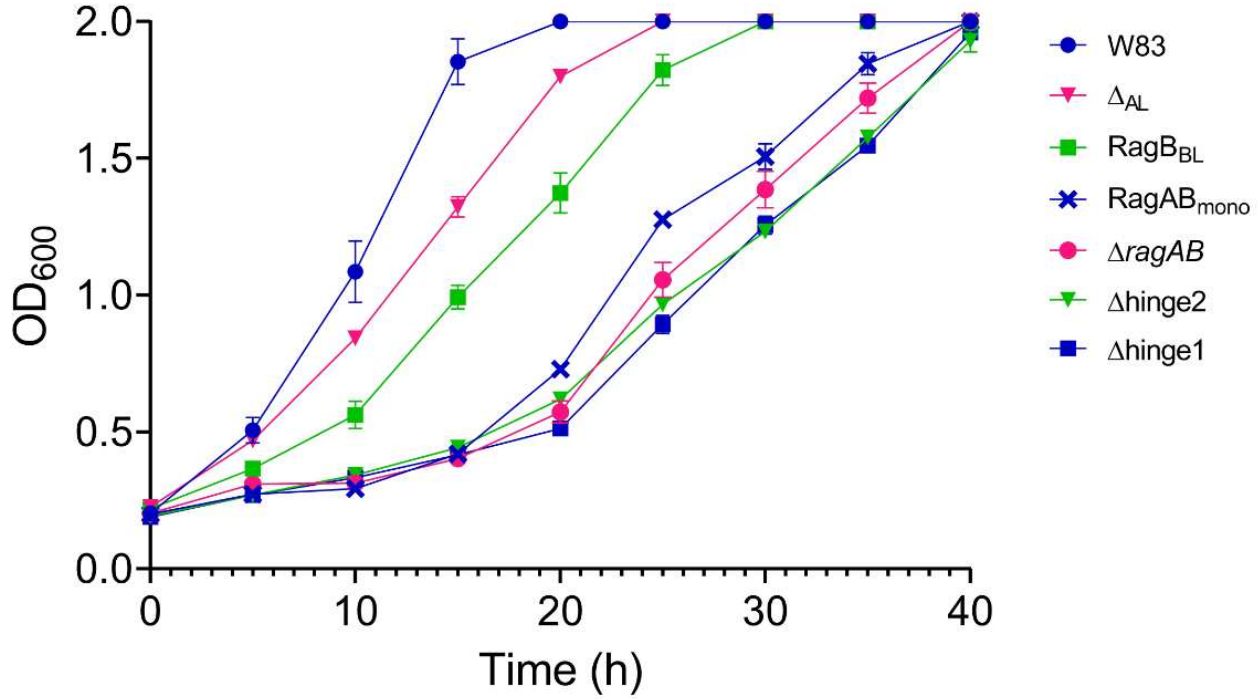
2.0
1.5
1.0
0.5
0.0
OD600
0
10
20
30
40
Time (h)
W83
ΔAL
RagBBL
RagABmono
ΔragAB
Δhinge2
Δhinge1

b

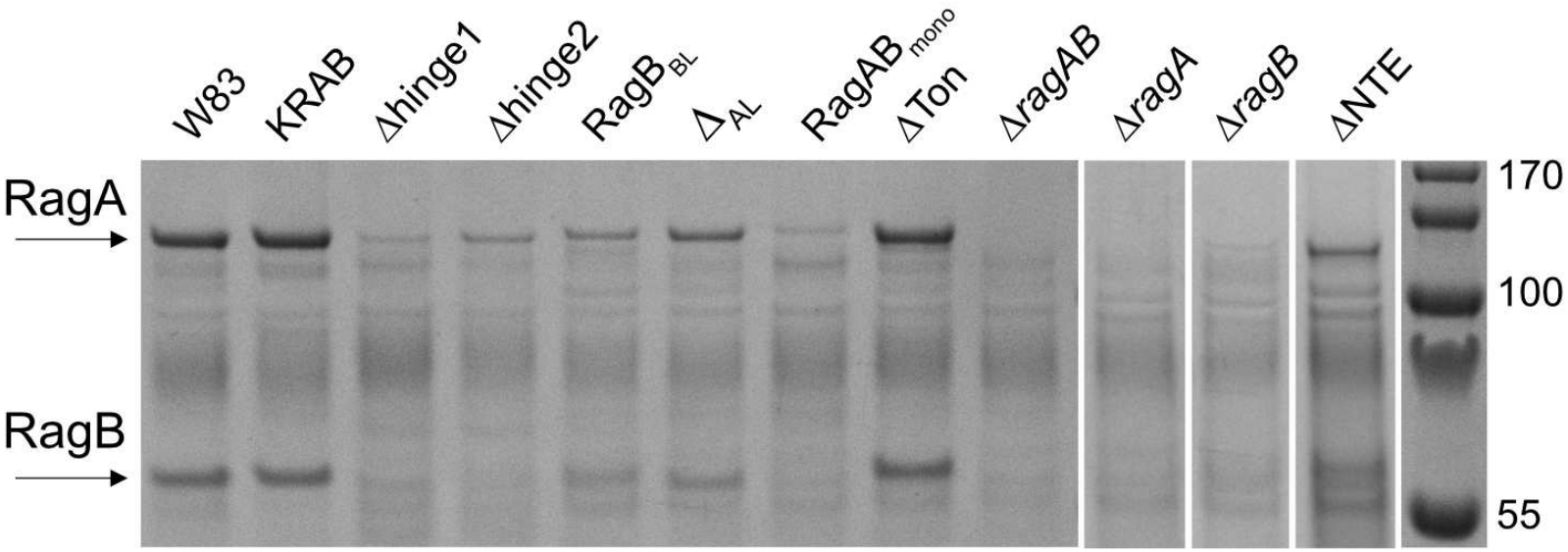
W83
KRAB
Δhinge1
Δhinge2
RagBBL
ΔAL
RagABmono
ΔTon
ΔragAB
ΔragA
ΔragB
ΔNTE
RagA
RagB
170
100
55

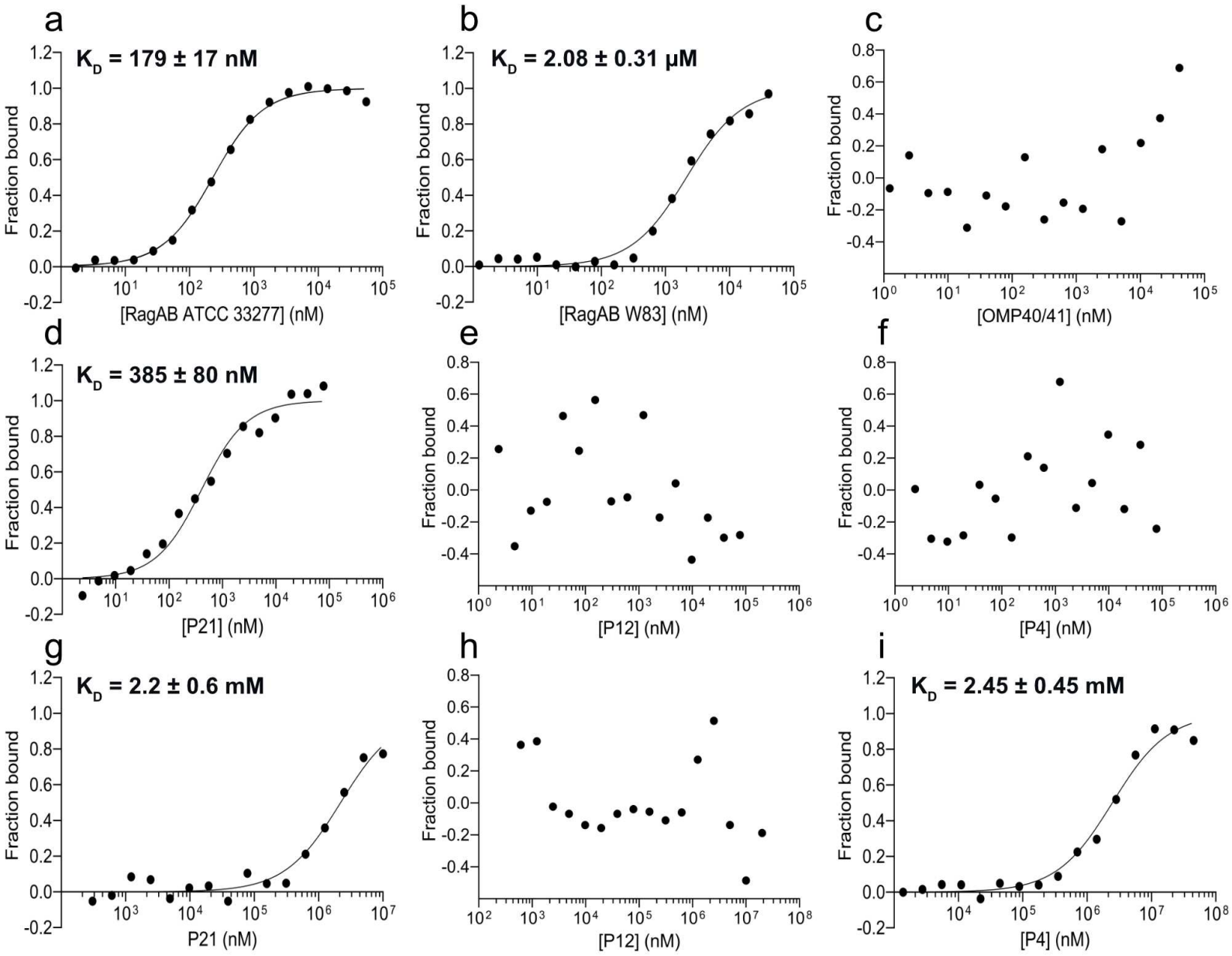
a
K_D = 179 ± 17 nM
Fraction bound
[RagAB ATCC 33277] (nM)
b
K_D = 2.08 ± 0.31 μM
Fraction bound
[RagAB W83] (nM)
c
Fraction bound
[OMP40/41] (nM)
d
K_D = 385 ± 80 nM
Fraction bound
[P21] (nM)
e
Fraction bound
[P12] (nM)
f
Fraction bound
[P4] (nM)
g
K_D = 2.2 ± 0.6 mM
Fraction bound
P21 (nM)
h
Fraction bound
[P12] (nM)
i
K_D = 2.45 ± 0.45 mM
Fraction bound
[P4] (nM)

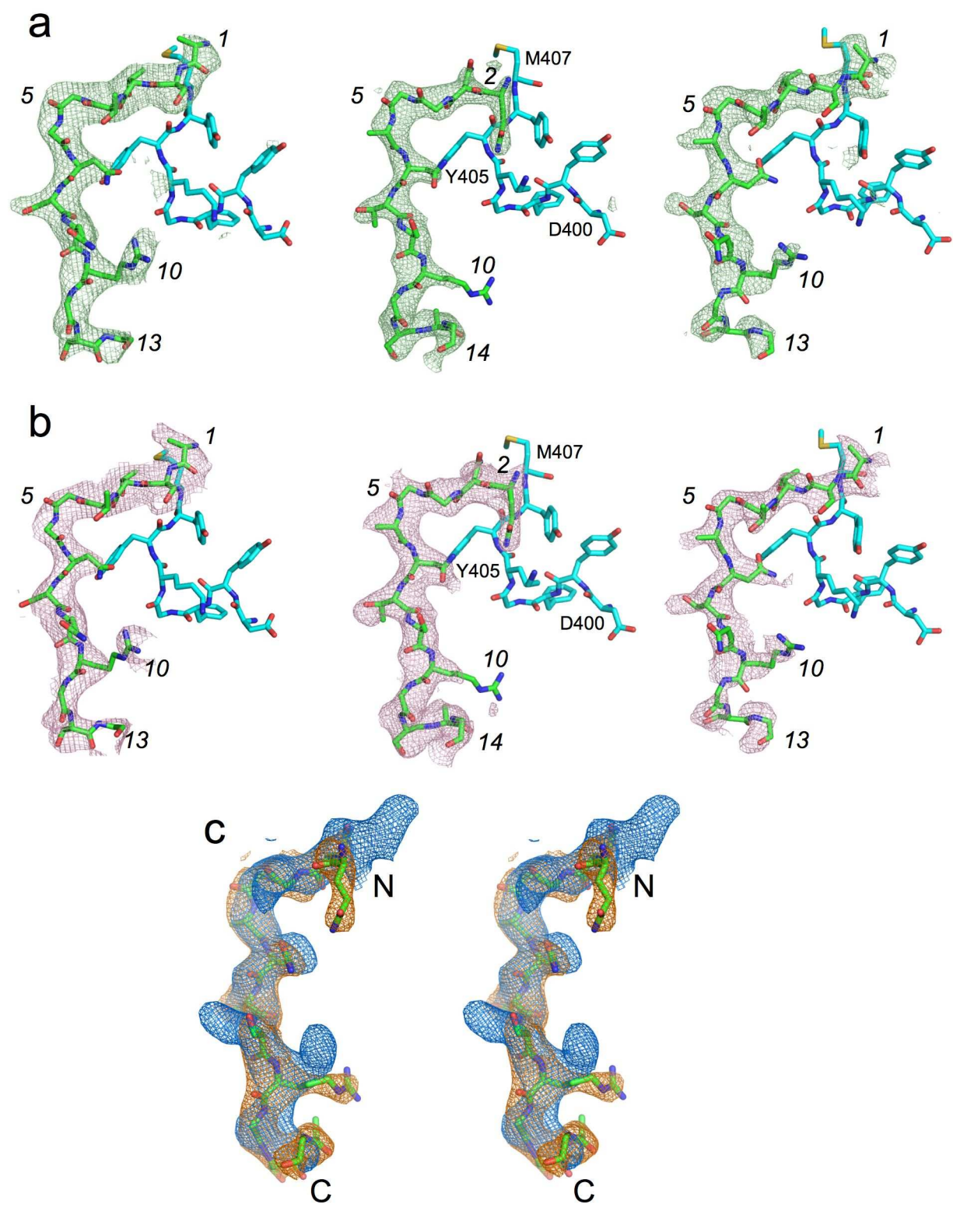
a
1
5
10
13
M407
2
5
Y405
D400
10
14
1
5
10
13
b
1
5
10
13
M407
2
5
Y405
D400
10
14
1
5
10
13
c
N
C
N
C

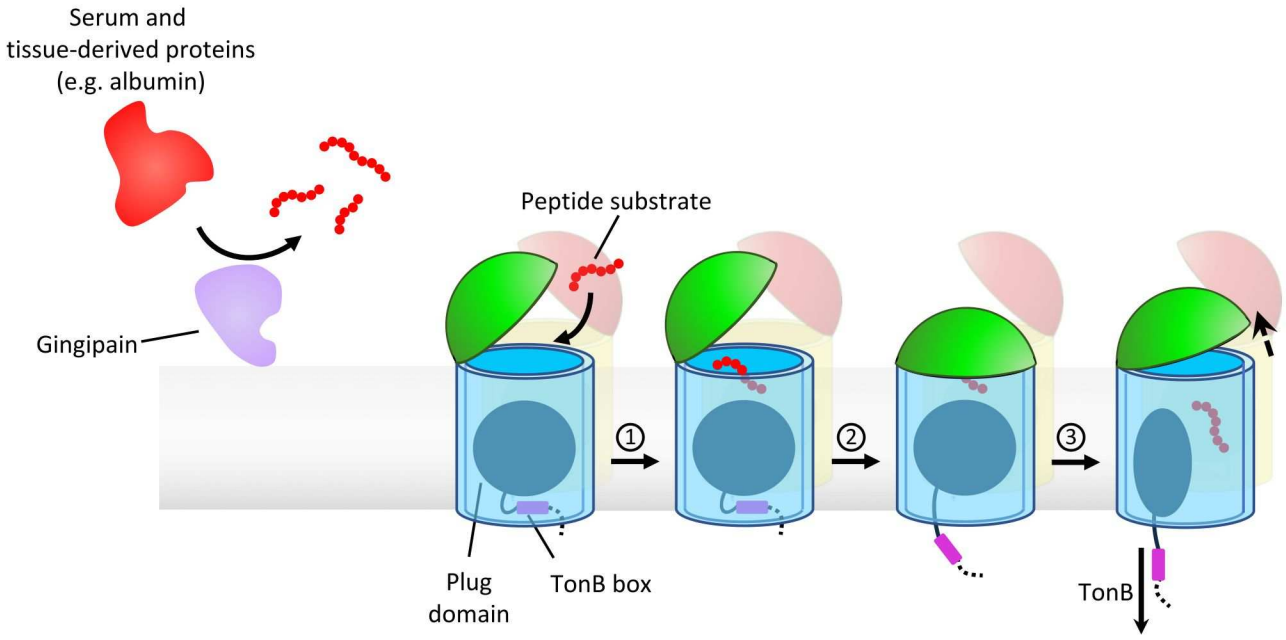
Serum and
tissue-derived proteins
(e.g. albumin)
Gingipain
Peptide substrate
①
②
③
Plug
domain
TonB box
TonB

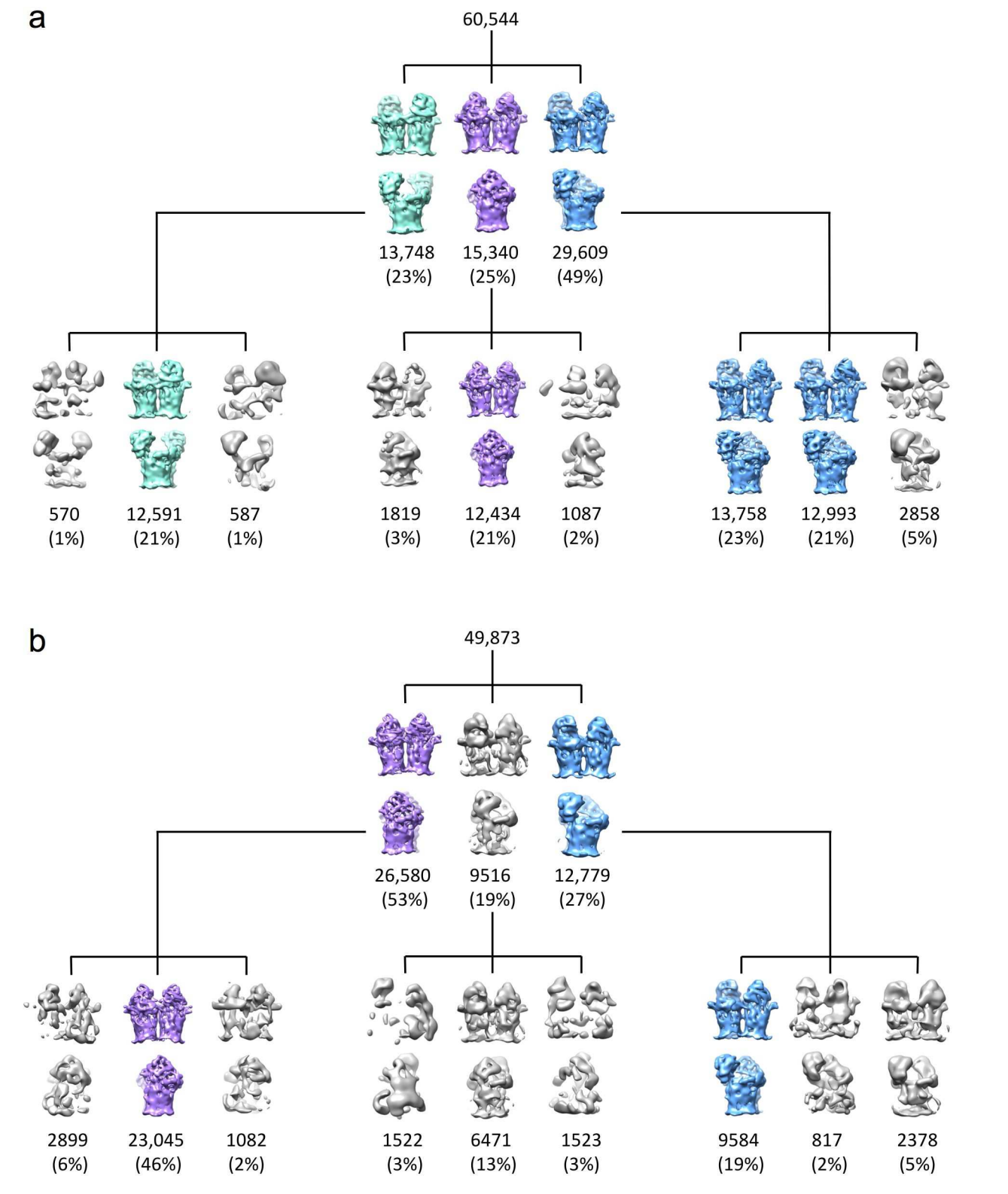
a
60,544
13,748
(23%)
15,340
(25%)
29,609
(49%)
570
(1%)
12,591
(21%)
587
(1%)
1819
(3%)
12,434
(21%)
1087
(2%)
13,758
(23%)
12,993
(21%)
2858
(5%)
b
49,873
26,580
(53%)
9516
(19%)
12,779
(27%)
2899
(6%)
23,045
(46%)
1082
(2%)
1522
(3%)
6471
(13%)
1523
(3%)
9584
(19%)
817
(2%)
2378
(5%)